EXPERIMENTAL VALIDATION OF A NUMERICAL CONTROLLER USING CONVEX OPTIMIZATION WITH LINEAR MATRIX INEQUALITIES ON A QUARTER-CAR SUSPENSION SYSTEM

A Thesis

by

ROHIT HARI CHINTALA

Submitted to the Office of Graduate Studies of
Texas A&M University
in partial fulfillment of the requirements for the degree of

MASTER OF SCIENCE

August 2011

Major Subject: Mechanical Engineering

EXPERIMENTAL VALIDATION OF A NUMERICAL CONTROLLER USING CONVEX OPTIMIZATION WITH LINEAR MATRIX INEQUALITIES ON A QUARTER-CAR SUSPENSION SYSTEM

A Thesis

by

ROHIT HARI CHINTALA

Submitted to the Office of Graduate Studies of
Texas A&M University
in partial fulfillment of the requirements for the degree of

MASTER OF SCIENCE

Approved by:

Chair of Committee,	Won-jong Kim
Committee Members,	Bryan Rasmussen
	Mehrdad Ehsani
Head of Department,	Dennis O'Neal

August 2011

Major Subject: Mechanical Engineering

ABSTRACT

Experimental Validation of a Numerical Controller Using Convex Optimization with Linear Matrix Inequalities on a Quarter-Car Suspension System. (August 2011)

Rohit Hari Chintala, B.E., Birla Institute of Technology

Chair of Advisory Committee: Dr. Won-jong Kim

Numerical methods of designing control systems are currently an active area of research. Convex optimization with linear matrix inequalities (LMIs) is one such method. Control objectives like minimizing the H_2, H_∞ norms, limiting the actuating effort to avoid saturation, pole-placement constraints etc., are cast as LMIs and an optimal feedback controller is found by making use of efficient interior-point algorithms. A full-state feedback controller is designed and implemented in this thesis using this method which then forms the basis for designing a static output feedback (SOF) controller. A profile was generated that relates the change in the SOF control gain matrix required to keep the same value of the generalized H_2 norm of the transfer function from the road disturbance to the actuating effort with the change in the sprung mass of the quarter-car system. The quarter-car system makes use of a linear brushless permanent magnet motor (LBPMM) as an actuator, a linear variable differential transformer (LVDT) and two accelerometers as sensors for feedback control and forms a platform to test these control methodologies.

For the full-state feedback controller a performance measure (H_2 norm of the transfer function from road disturbance to sprung mass acceleration) of 2.166×10^3 m/s^2 was achieved ensuring that actuator saturation did not occur and that all poles had a minimum damping ratio of 0.2. The SOF controller achieved a performance measure of 1.707×10^3 m/s^2 ensuring that actuator saturation does not occur. Experimental and simulation results are provided which demonstrate the effectiveness of the SOF controller for various values of the sprung mass. A reduction in the peak-to-peak velocity by 73%, 72%, and 71% was achieved for a sprung mass of 2.4 kg, 2.8 kg, and 3.4 kg, respectively. For the same values of the sprung mass, a modified lead-lag compensator achieved a reduction of 79%, 77% and, 69%, respectively. A reduction of 76% and 54% in the peak-to-peak velocity was achieved for a sprung mass of 6.0 kg in simulation by the SOF controller and the modified lead-lag compensator, respectively. The gain of the modified lead-lag compensator needs to be recomputed in order to achieve a similar attenuation as that of the SOF controller when the value of the sprung mass is changed. For a sprung mass of 3.4 kg and a suspension spring stiffness of 1640 N/m the peak-to-peak velocity of the sprung mass was attenuated by 42 %.

ACKNOWLEDGMENTS

I would sincerely like to thank my committee chair Dr. Won-jong Kim for being a mentor and providing valuable insight and guidance through every step of my research. I would also like to thank the committee members Dr. Bryan Rasmussen and Dr. Mehrdad Ehsani for their help in completing my research.

I am grateful to former students Mr. Seungho Lee, Mr. Bryan Murphy and Mr. Justin Allen whose work formed the basis of my research. I would also like to thank my friends in the research lab who made my research experience enjoyable. Last but not the least, I would like to thank my family for their tremendous support and love.

TABLE OF CONTENTS

LIST OF FIGURES

Page

Page

LIST OF TABLES

CHAPTER I

INTRODUCTION

The function of an active suspension system in a vehicle is twofold – ride handling that enables the driver to maintain control of the vehicle and ride comfort that minimizes the road disturbances being transmitted to the passengers. This thesis deals with the latter function with the design and implementation of real-time controllers using convex optimization with LMIs. Active suspension systems could handle ride-comfort requirements better than passive suspension. They employ an actuator powered by an external source to minimize the sprung mass acceleration. The control algorithms are designed that calculate the optimum actuating force required to minimize the sprung-mass acceleration making use of the input data from sensors.

A. Background and Motivation

A quarter-car active suspension system was constructed by Allen [1] to serve as a test bed for applying various control methodologies. The various components of the quarter-car model are shown in Figure 1. It consists of a sprung mass and an unsprung mass supported on a wheel that rotates on a cam that simulates road disturbance. An LVDT and two accelerometers are used as sensors. This test bed incorporates the LBPMM developed by Murphy [2] as the actuator. Magnetic actuation by this LBPMM reduces the response time, enabling the use of faster controllers. This linear motor

_____

This thesis follows the style of *IEEE Transactions on Control Systems Technology*.

eliminates the need for using rotating machinery making the actuator ideal for use in active suspension control. Lee [3] designed four separate controllers using modified lead-lag, linear-quadratic (LQ) servo with Kalman filter, fuzzy control, and slide mode control (SMC) and was able to achieve an attenuation of 78% on the sprung mass velocity on the quarter-car test bed.

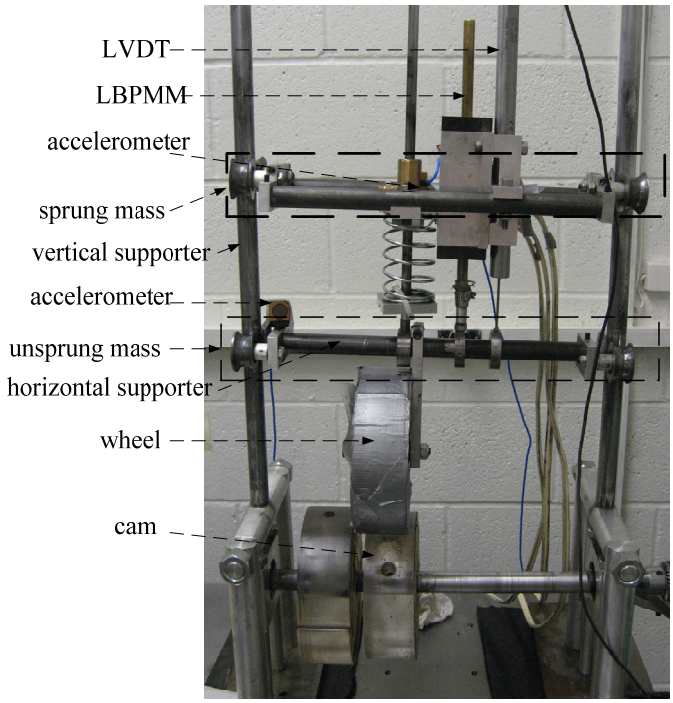

Figure 1. Photograph of the quarter-car test bed with active suspension [1]

Several classical control methodologies such as linear quadratic Gaussian/loop transfer recovery (LQG/LTR), lead-lag control, etc. depend on intuition and design iterations. In order to reduce trials and errors and also to make the most of the recent advances in computational powers of computers, research in control systems currently focuses on numerical methods to come up with an optimal controller that can satisfy

various design objectives. LMIs have emerged as a powerful tool in this regard [4]. Various problems in control theory can be represented as LMIs which can then be solved by convex optimization [4]. Efficient interior-point algorithms such as those presented in [5] are able to solve the convex optimization problems in polynomial time. The algorithm in [5] was incorporated in the LMI control toolbox of MATLAB [6] where the LMIs can be defined and solved. This toolbox is utilized in this thesis to solve the convex optimization problem.

In addition to guaranteed stability of the physical system, the objective of the controller may also be to achieve several time- and frequency-domain specifications such as peak time, settling time, minimizing H_2 and H_∞ norms, pole placements, etc. Each of these control objectives can be cast as LMIs [7], [8]. A certain amount of conservatism is introduced into the design by relating these LMIs with a single variable that enables us to setup a convex optimization problem [9] which can then be solved through one of the interior-point algorithms described in [5].

This research aims at validating the above control methodology by applying the full-state feedback controller (FSF) on the quarter-car suspension test bed [1]. The primary control objective is to minimize the H_2 norm of the transfer function from the road disturbance to the sprung-mass acceleration. Key constraints such as limiting the actuating force and constraining the placement of poles for optimum dynamic performance are also incorporated. One of the main advantages that this method offers is that, the controller need not be redesigned even when there are changes in the parameters

such as the sprung mass, suspension spring stiffness etc. The convex optimization program is rerun with the new parameter values.

FSF is rarely achieved in real-world systems. It becomes necessary to design a feedback controller dependent on the available measurements of the output. Hence, this research also looks into the current numerical methods to design an SOF controller. The problem of finding an SOF controller that achieves the desired performance characteristics or determines that such a feedback controller does not exist, is an important open question in control theory [10]. Unlike FSF control, the optimization problem for designing an SOF controller is not convex with the numerical methods providing only a suboptimal solution [11]. It is an important control problem, however, as an SOF controller is one of the simplest controllers to implement since it requires no estimator and just involves multiplying the output states by a constant numeric value.

A survey of several numerical output-feedback control-design methods is presented in [12]. It is possible to classify these numerical controllers into three classes – nonlinear programming methods, parametric optimization methods, and convex programming methods [12]. Non-smooth, non-convex optimization methods such as those presented in [13], [14] are currently considered as the most numerically efficient algorithms for SOF stabilization and closed-loop performance guarantees [15]. The Levine-Athans' primal method [16] and the Levine-Athans dual method [17] obtain a local optimal solution through an iterative procedure involving the solution of nonlinear equations. Optimization methods such as the Min-Max Algorithm [18] and Product Reduction Algorithm [19] try to solve the inequality constraint associated with SOF

control through a parametric approach. In this thesis an algorithm based on [15] is developed and implemented on the quarter-car test bed. This method can be classified as a mixture of convex programming method where additional constraints are added to make the SOF problem convex. In this method, the problem of converting the SOF design problem into a convex optimization problem is achieved by applying the elimination lemma and introducing slack variables. In this thesis an additional constraint of limiting the actuating effort is applied to this method and tested for different values of the sprung mass. The attenuation of the sprung mass acceleration achieved through this method is then compared with that of the modified lead-lag controller. A method to find a global optimal SOF control matrix is investigated in [20] and [21].

B. Contribution of the Thesis

Multi-objective FSF controllers have been designed in [22] and [23] using convex optimization with LMIs. In this thesis the same principle is used to design and implement the FSF controller for the quarter-car test bed. Using the FSF control gain matrix an SOF controller is designed based on the algorithm in [15]. The main aim of this thesis is to validate this SOF control algorithm. However, the control algorithm provided in [15] does not constrain the available actuating effort. The control algorithm is modified so that the SOF controller accounts for actuator saturation. A relationship between the sprung mass and the entries of the SOF gain matrix is found. Using this relationship, the modified SOF control algorithm is implemented for three different values of the sprung mass. A comparison of this performance is made with the modified lead-lag controller developed by Lee [3]. With the help of simulation and experimental

results it is shown that the gain of the modified lead-lag compensator needs to be recomputed in order to achieve a similar reduction in the peak-to-peak velocity of the sprung mass as that of the modified SOF controller.

C. Overview of the Thesis

This thesis consists of six chapters. In the second chapter, the various components of the quarter-car test bed is given. In Chapter III, a background of the control theory used to design the full state feedback and SOF controllers is given. Chapter IV contains a description of the step-by-step procedure followed to come up with the controllers and also the experimental and simulation results. Chapter V consists of the analysis of the obtained results. A comparison is also made with the modified lead-lag controller designed by Lee [3]. Chapter VI presents a summary of the thesis, conclusions, and the future work that can be done in this area.

CHAPTER II

EXPERIMENTAL SETUP

The experimental setup shown in Figure 1 was developed by Allen [1]. The setup was built in order to simulate a quarter-car suspension system. The quarter-car system can be divided into two main parts—sprung mass (the portion of the car that lies above the suspension spring) and the unsprung mass (including the unsprung mass block and the wheel). A cam driven by a variable-speed electrical drill is used to simulate the road disturbance. Three sensors (2 accelerometers and an LVDT) are mounted on the setup, which constantly provide real-time data that can be used for feedback control. An LBPMM is also mounted on the system which serves as a direct-drive linear actuator providing the necessary force to minimize the sprung mass vibration.

Figure 2 provides a schematic description of the system. . A schematic of the control architecture is shown in Figure 3. The data collected from the sensors are used by the feedback controller which computes the actuating force required to minimize the sprung mass vibration. The DS1104 digital-signal-processing control board from dSPACE Inc. enable real-time data to be acquired from the sensors through 16-bit A/D channels. Through its 16-bit D/A channels control signals can be sent to the actuator. The output from the D/A channels is amplified by the three PWM amplifiers Model 12A8K from Advanced Motion Controls to provide a current in the range of ±6 A to each phase of the LBPMM.

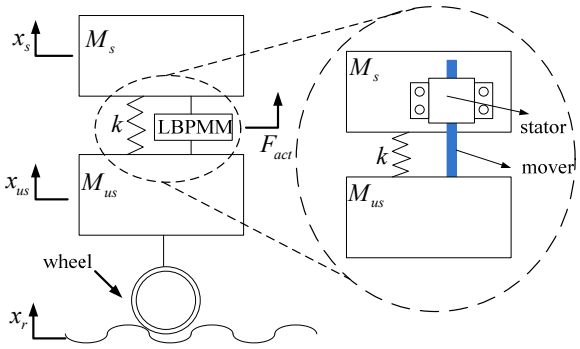

Figure 2. Schematic of the quarter car suspension system [3]

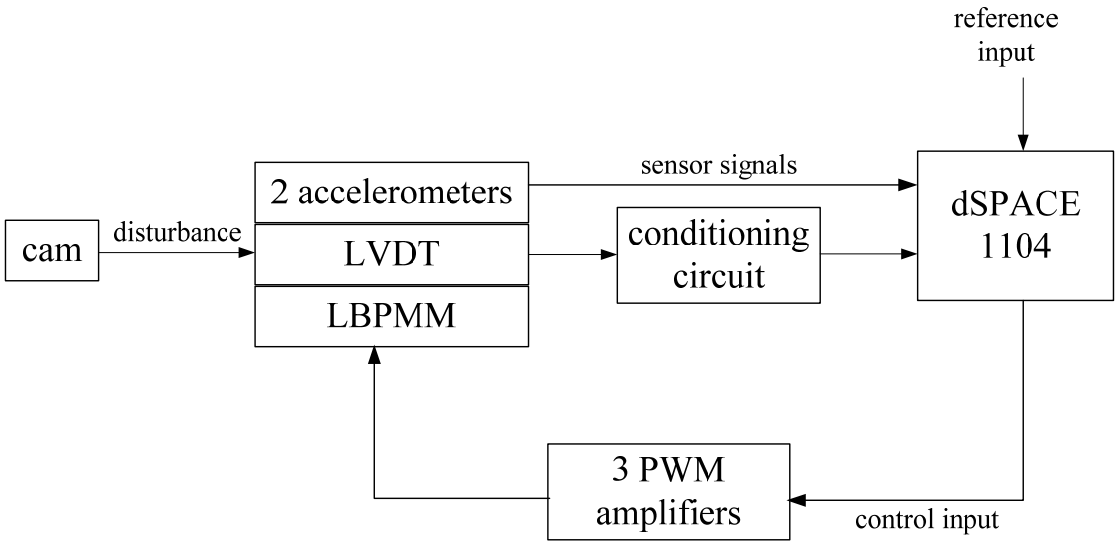

Figure 3. Schematic of the control architecture [3]

A brief description of the individual components used in the model is described below.

A. Linear Brushless Permanent-Magnet Motor

A schematic diagram of the LBPMM developed by Murphy [2] is shown in Figure 4. The motor works on the principle that a force is induced in the current carrying conductor placed in a magnetic field. The actuator incorporates a new design where the magnets which are encased in a brass tube (mover), are arranged in NS-NS—SN-SN

orientation. This placement of the magnet pieces generates a greater magnetic flux density near the like poles. The stator consists of a three phased coil. By controlling the amount of current passing through each of these coils the total force generated by the actuator can be controlled as governed by the commutation law (1) [2] given as follows:

$$\begin{bmatrix} i_a(t) \\ i_b(t) \\ i_c(t) \end{bmatrix} = C \begin{bmatrix} 2 & 0 \\ 1 & \sqrt{3} \\ -1 & \sqrt{3} \end{bmatrix} \begin{bmatrix} \cos \gamma_1 z_o \\ \sin \gamma_1 z_0 \end{bmatrix} f_{zd}(t). \tag{1}$$

In (1), $i_a(t)$, $i_b(t)$, and $i_c(t)$ are the currents passing through the three-phase coil, z_0 is the relative displacement between the mover and the stator, $\gamma_1 = \left| \frac{2\pi}{l} \right|$ where l is the pitch of the actuator and $f_{zd}(t)$ is the required force in the axial direction. The constant C was determined experimentally and was found to be equal to 0.1383 A/N [1].

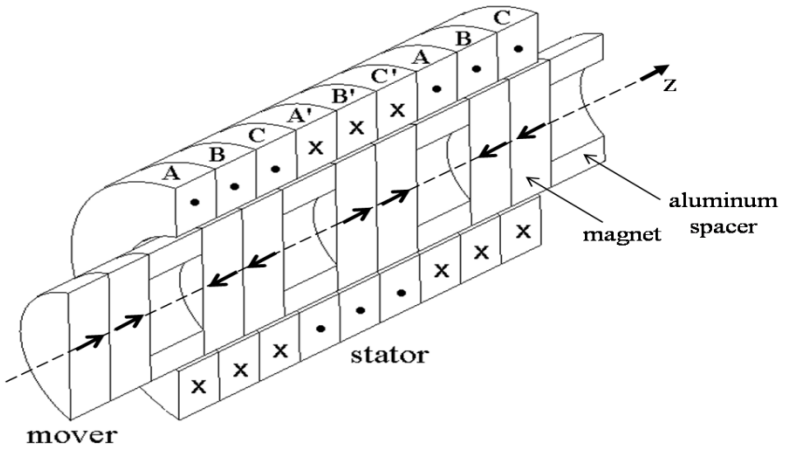

Figure 4. Schematic diagram of LBPMM [1]

B. Linear Variable Differential Transformer (LVDT)

The LVDT (Schaevitz DC-SE 4000) is mounted in order to receive real-time data of the relative displacement between the sprung and unsprung masses. The input to the LVDT (10V) was provided by the Agilent 3644 A power supply. The output voltage of the LVDT had a range between 0 and 5 V. In order to make it compatible with the dSPACE 1104 control board with a voltage swing from 10 to − 10V, the output from the LVDT was fed to a signal conditioning circuit shown in Figure 5 [3].

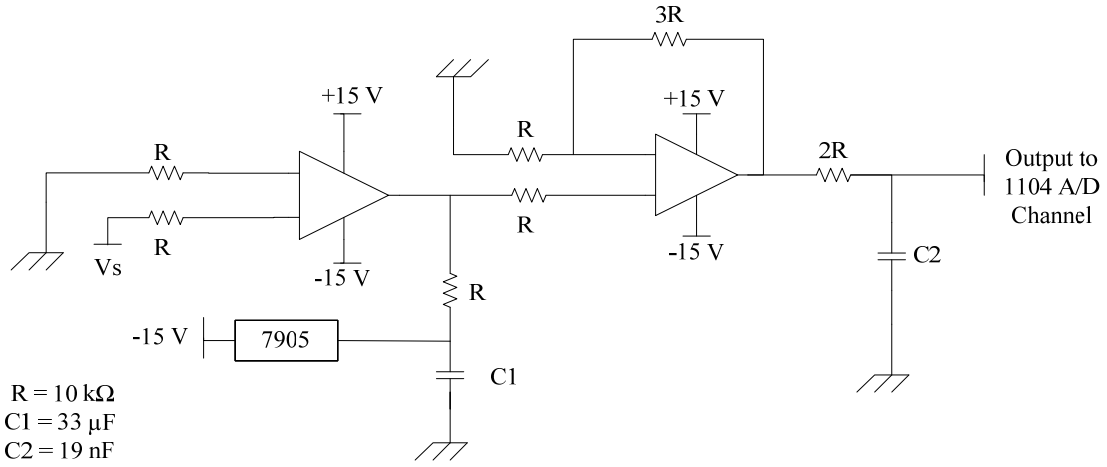

Figure 5. Schematic diagram of the conditioning circuit [3]

C. Accelerometers

Two accelerometers (Piezotronics model 355B04) were mounted on the system in order to receive real-time data of the sprung- and unsprung-mass accelerations. The accelerometers have an effective frequency range from 1 Hz to 10 KHz and a sensitivity

of 1007 mV/g. The accelerometers are powered by a signal conditioner (PCB model 482A22).

D. Sprung Mass, Unsprung Mass, Wheel and Suspension Spring

The parameters which ultimately define the dynamics of the system are shown in Table 1. The parameters m_s, m_{us}, and k represent the sprung mass, unsprung mass and the suspension spring stiffness respectively. In order to account for the frictional force on the sprung mass the damping coefficient c is introduced. The wheel which is covered by a tire made of natural isoprene can be modeled as a spring and a viscous damper with values k_w and c_w respectively. The values of these parameters were found by simulation and experimental results [3].

Table I

Parameters and corresponding values of the quarter-car system [3]

Parameters	Values
m_s	2.80 kg
m_{us}	2.28 kg
k	840 N/m
c	17 N-s/m
c_w	15 N-s/m
k_w	3500 N/m

CHAPTER III

CONTROL DESIGN BASED ON CONVEX OPTIMIZATION

Consider the state-space representation of a physical plant L given as follows:

$$\begin{aligned} \dot{x} &= Ax + B_u u + B_1 w \\ z_1 &= C_1 x + D_1 u \\ z_2 &= C_2 x + D_2 u \\ y &= Cx. \end{aligned} \tag{2}$$

In (2), x is the state vector, u is the control vector, w is the disturbance vector, z_1 is the performance measure, z_2 is the constrained output, and y is the measured output respectively. It is required that a feedback control gain matrix K be designed so that it not only ensures stability of the plant L, but also guarantees certain performance characteristics. The control effort would then be as shown in (3) as follows:

$$u = KCx. \tag{3}$$

The closed-loop representation of the system L is then as shown in (4) as follows:

$$\begin{aligned} \dot{x} &= A_{cl} x + B_1 w \\ z_1 &= C_{cl1} x \\ z_2 &= C_{cl2} x. \end{aligned} \tag{4}$$

where $A_{cl} = A + B_u KC$, $C_{cl1} = C_1 + D_1 KC,$ and $C_{cl2} = C_2 + D_2 KC$. For the special case of FSF control, C is an identity matrix.

A. Full-State Feedback Controller

In this thesis the plant L represents the quarter-car active suspension test bed. The control objectives are presented in this subsection. The primary objective is to

design a controller to minimize the H_2 norm of the transfer function $H(s)$ from the road disturbance to the performance measure (sprung mass acceleration). The H_2 norm was selected to serve as a measure of the ride comfort [9] and can be interpreted as the square root of the total output energy when a unit impulse is given to the system. The H_2 norm in the frequency domain is as defined in (5) as follows:

$$\|H\|_2 = \sqrt{\frac{1}{2\pi}\int_{-\infty}^{\infty} tr(H(j\omega) * H(j\omega))d\omega}. \tag{5}$$

The square of the H_2 norm can also be represented in terms of the state-space matrices given in (2) as follows:

$$\|h(t)\|_2^2 = tr(C_{cl1} S_0 C_{cl1}{}^T), \tag{6}$$

where S_0 is the solution to

$$A_{cl} S_0 + S_0 A_{cl}^T + B_1 B_1^T = 0 \tag{7}$$

and $h(t)$ is the impulse response of the transfer function $H(s)$ [8].

The equation given in (6) can be derived by the following method. The transfer function $H(s)$ is defined as follows:

$$H(s) = C_{cl1}(sI - A_{cl})^{-1} B_1 . \tag{8}$$

The impulse response matrix $h(t)$ of the plant is found by taking the inverse Laplace transform of the transfer function $H(s)$ shown as follows:

$$h(t) = L^{-1}\{C_{cl}(sI - A_{cl})^{-1} B_1\} = C_{cl1} e^{A_{cl} t} B_1. \tag{9}$$

By Parseval's theorem, the second-order transfer function norm $\|H(s)\|_2$ in the frequency domain is equal to the second-order impulse response norm $\|h(t)\|_2$ in the time domain [21]. If h_{ij} represents the element in the i^{th} row and j^{th} column in the matrix $h(t)$ then the H_2 norm can also be written as

$$\|h(t)\|_2^2 = \int_0^\infty \sum_{ij} h_{ij}(t)^2 dt = \int_0^\infty tr\{h(t)h(t)^T\}dt. \tag{10}$$

From (9), (10) can also be written as

$$\|h(t)\|_2^2 = \int_0^\infty tr\{C_{cl1}e^{A_{cl}t}B_1B_1^T e^{A_{cl}{}^T t}C_{cl1}{}^T\}dt = tr\{C\int_0^\infty e^{At}B_1B_1^T e^{A^T t}dtC^T\}. \tag{11}$$

By defining

$$S_0 = \int_0^\infty e^{At}B_1B_1{}^T e^{A^T t}dt \tag{12}$$

in (11), we get (6), as S_0 is the controllability gramian which is the unique solution of (7). Hence with the help of (6) and (7), the H_2 norm of $H(s)$ can be represented in terms of the state-space matrices in (2).

In the implementation of the feedback controller, it must also be ensured that the actuating force must not exceed the saturation limit of the actuator, the LBPMM in our case. Failure to do so would result in excessive current, which might demagnetize the magnets in the actuator. To ensure the above time-dependent hard constraint, the generalized H_2 norm $\|H\|_g$ defined in (13) is used [9]. $\|H\|_g$ represents the peak

amplitude of the constrained output z_2 when a unit energy input from the disturbance vector w is fed to the system and is represented as follows:

$$\|H\|_g = \sup\left\{\|z_2(t)\| : x(0) = 0, t \geq 0, \int_0^t \|w(\tau)\|^2 \, d\tau \leq 1\right\}. \tag{13}$$

Another constraint that is added while designing the controller is to restrict the placement of the closed-loop poles in the complex plane. The location of the poles determines time-domain characteristics such as settling time, rise time, etc. Although the poles deep in the left-half complex plane increase stability, these very fast poles are difficult to model. After identifying the control objectives as listed above, the next step in the design process is to represent them as LMIs. An LMI has the following form

$$F(r) = F_0 + \sum_{i=1}^{m} r_i F_i > 0, \tag{14}$$

where F_i are constant symmetric matrices in the real space $\mathbb{R}^{n\times n}$ and r is a variable matrix which belongs to $\mathbb{R}^{m\times 1}$ [4] containing the variables r_i. The inequality $F(x) > 0$ implies that the matrix is positive definite, i.e. the real part of all the eigen values of $F(x)$ are greater than zero. The LMI as shown in (15)

$$\begin{bmatrix} Q(r) & S(r) \\ S(r)^T & R(r) \end{bmatrix} > 0 \tag{15}$$

is another form of representing (14), where $Q(r)$, $S(r)$, and $R(r)$ are symmetric matrices affinely dependent on r [4]. By Schur complements, (16) is equivalent to the following nonlinear convex inequalities [4]:

$$Q(x) > 0\ ,\ Q(x) - S(x)R(x)^{-1}S(x)^{T} > 0. \tag{16}$$

Now we try to represent the control objectives in the form of (15). If we let the H_2 norm be less than or equal to some positive value γ, then the control objective would be equivalent to minimizing the value of γ. We introduce a variable symmetric matrix S [5] such that

$$S > 0; \quad A_{cl}S + SA_{cl}^{T} + B_1 B_1^{T} < 0. \tag{17}$$

By subtracting the equation in (7) from the inequality in (17) we get

$$A_{cl}(S - S_0) + (S - S_0)A_{cl}^{T} < 0. \tag{18}$$

Lyapunov inequality states that a system represented by the state space equation $\dot{x}_a = A_1 x_a$ is asymptotically stable if and only if there exists a symmetric matrix P such that

$$A_1^{T}P + PA_1 \le 0\ ;\ P > 0. \tag{19}$$

Since A_{cl} is to be stabilized through feedback control, from (18) we can say that $S - S_0$ must be positive definite i.e.

$$S - S_0 > 0. \tag{20}$$

From (20) we get

$$\begin{aligned} & tr\{C_{cl}(S - S_0)C_{cl}^{T}\} > 0 \\ & \Rightarrow tr\{C_{cl1}S_0 C_{cl1}^{T}\} < tr\{C_{cl1}SC_{cl1}^{T}\} \\ & \Rightarrow \|h(t)\|_2^2 < tr\{C_{cl1}SC_{cl1}^{T}\}. \end{aligned} \tag{21}$$

From (21) it is clear that if $tr\{C_{cl1}SC_{cl1}^{T}\} < \gamma,$ then the H_2 norm of $H(s)$ would also be less than equal to γ. The inequalities (17) and (21) can now be setup as LMIs by

introducing positive deifinte variable matrices $P_1 = S^{-1}$ and Q [9]. Using (15) and (16) we have

$$\begin{bmatrix} A_{cl}^T P_1 + P_1 A_{cl} & P_1 B_1 \\ B_1^T P_1 & -I \end{bmatrix} < 0 \; ; \begin{bmatrix} P_1 & C_{cl1} \\ C_{cl1}^T & Q \end{bmatrix} > 0 \; ; \; tr(Q) < \gamma. \tag{22}$$

The first matrix inequality ensures that the inequality in (18) is satisfied. From the second matrix inequality in (22) we get

$$\begin{aligned} & P_1 > 0 \\ \Rightarrow & S > 0 \end{aligned} \tag{23}$$

and

$$\begin{aligned} & Q - C_{cl1} P^{-1} C_{cl1}^T > 0 \\ \Rightarrow & tr(C_{cl1} S C_{cl1}^T) < tr(Q) < \gamma. \end{aligned} \tag{24}$$

Thus the LMI in (22) ensures that the H_2 norm is less than γ.

It is required that the generalized H_2 norm as described in (13) for the plant L must be less than some positive value ν in order to avoid actuator saturation. This value of ν determines the maximum control effort that can be utilized when a unit energy disturbance enters the system. In order to represent this objective as an LMI, a Lyapunov function is first defined as follows [5]:

$$V(x_{cl}) = x^T P_2 x \tag{25}$$

where P_2 is a symmetric positive definite matrix. Differentiating (25) we get

$$\frac{d}{dt}V(x) = \dot{x}^T P_2 x + x^T P_2 \dot{x}. \tag{26}$$

Using (4), (26) can be written as follows:

$$\frac{d}{dt}V(x) = \begin{bmatrix} x \\ w \end{bmatrix}^T \begin{bmatrix} A_{cl}^T P_2 + P_2 A_{cl} & P_2 B_1 \\ B_1^T P_2 & 0 \end{bmatrix} \begin{bmatrix} x \\ w \end{bmatrix}$$

$$\frac{d}{dt}V(x) - \begin{bmatrix} x \\ w \end{bmatrix}^T \begin{bmatrix} 0 & 0 \\ 0 & -I \end{bmatrix} \begin{bmatrix} x \\ w \end{bmatrix} = \begin{bmatrix} x \\ w \end{bmatrix}^T \begin{bmatrix} A_{cl}^T P_2 + P_2 A_{cl} & P_2 B_1 \\ B_1^T P_2 & -I \end{bmatrix} \begin{bmatrix} x \\ w \end{bmatrix}. \tag{27}$$

From (27) the following condition holds true:

$$\begin{bmatrix} A_{cl}^T P_2 + P_2 A_{cl} & P_2 B_1 \\ B_1^T P_2 & -I \end{bmatrix} < 0 \Rightarrow \frac{d}{dt}V(x) - ww^T < 0. \tag{28}$$

Integrating (28) we get

$$V(x(\tau)) < \int_0^\tau ww^T dt. \tag{29}$$

Our objective is to ensure that for any time $\tau > 0$ the constrained output z_2 be such that $z_2(\tau)^T z_2(\tau) < \nu \int_0^\tau ww^T dt$. This ensure that when a energy disturbance less than unity $(\int_0^\tau ww^T dt < 1)$ enters the system, z_2 does not exceed $\sqrt{\nu}$. From (29) it is sufficient if

$$\begin{aligned} &z(\tau)^T z(\tau) < \nu V(x(\tau)) \\ &\Rightarrow x^T (C_{cl2}^T C_{cl2} - \nu P_2) x < 0. \end{aligned} \tag{30}$$

The inequality (30) can be represented as the following LMI:

$$\begin{bmatrix} P_2 & C_{cl2}^T \\ C_{cl2} & \nu I \end{bmatrix} > 0. \tag{31}$$

In order to establish the third constraint that is restricting the location of the closed loop poles in the complex plan, a convex LMI region is defined as shown below [7]:

$$D = \{z \in C : N + zM + zM^T\} \tag{32}$$

where N is symmetric matrix, and both N and M are fixed real matrices. If n_{ij} and m_{ij} correspond to general entries in the N and M matrices, respectively, then the plant L is D stable (the poles lie in the LMI region defined by D) under closed-loop feedback if and only if there exists a positive-definite matrix P_3 such that the following condition is satisfied [7]:

$$\left[n_{ij} P_3 + m_{ij} A_{cl}^T P_3 + m_{ji} P_3 A_{cl} \right]_{ij} < 0. \tag{33}$$

In order to convert these LMIs into a convex optimization problem with the objective of minimizing the value of γ, we need to equate the matrices P_1, P_2 and P_3 [5]. This introduces some conservatism in the design process. The following substitutions are then made in the LMIs in (22), (26), (29) and (31):

$$\begin{aligned} X &= P^{-1} \\ Y &= K_{sf} X. \end{aligned} \tag{34}$$

Representing the LMIs in (22), (31) and (33) in terms of the state-space matrices in (4) and making use of the substitutions in (34) we get the following inequalities:

$$\begin{bmatrix} AX + XA^T + B_u Y + Y^T B_u^T & B_1 \\ B_1^T & -I \end{bmatrix} < 0 \tag{35}$$

$$\begin{bmatrix} X & C_1 X + D_1 Y \\ XC_1^T + XD_1^T & Q \end{bmatrix} > 0 \; ; \; tr(Q) > \gamma \tag{36}$$

$$\begin{bmatrix} X & XC_2^T + Y^T D_2^T \\ C_2 X + D_2 Y & \nu I \end{bmatrix} > 0 \tag{37}$$

$$\left[n_{ij} X + m_{ij} (AX + B_u Y) + m_{ji} (XA^T + Y^T B_u^T) \right]_{ij} < 0. \tag{38}$$

The LMIs (35)—(38) are then defined using the LMI control toolbox in MATLAB [6]. The optimization variables are X , Y and γ . The convex optimization program is then run which finds the values of these variables that minimizes the value of γ at the same time ensuring that the constraints represented by the above LMIs are not violated. Once the optimal values of X and Y are found, the full-state feedback controller K_{sf} can be obtained from the substitutions in (34).

B. Static Output Feedback Controller

Since FSF is not always available in real-world systems, the available measurements must be used in order to design the feedback controller. The convexity in the case of the FSF optimization problem does not exist for SOF. No simple substitution as in (34) has been found for static output feedback problem [9]. However there exist some methods of obtaining a suboptimal solution for the SOF problem. In this research the algorithm as proposed in [15] has been used to design the SOF controller.

A parametric approach is used in [15] wherein by the process of applying the elimination lemma slack variables are introduced to convert the SOF design problem to a convex optimization problem. This enables an iterative procedure based on LMI optimization to be used, to converge to a local optimal solution.

In this approach the H_2 norm in (6) is expressed in terms of the observability gramian W_0 as follows:

$$\|h(t)\|_2^2 = Tr(C_{cl1} S_0 C_{cl1}^T) = Tr(B_1^T W_0 B_1). \tag{39}$$

Hence, analogous to the inequality in (17) we introduce a symmetric matrix W_1 such that the the following inequality is satisfied [15]:

$$W_1 > 0; A_{cl}^T W_1 + W_1 A_{cl} + C_{cl1}^T C_{cl1} < 0. \tag{40}$$

Expressing the inequality in (40) in terms of the state-space matrices in (4) we get the following:

$$(A + B_u K_{sof} C)^T W_1 + W_1 (A + B K_{sof} C) + (C_1^T + C^T K_{sof}^T D_1^T)(C_1 + D_1^T K_{sof} C) < 0. \tag{41}$$

A linear matrix function $M(W_1)$ is then defined [15] as follows:

$$M(W_1) = \begin{bmatrix} A^T W_1 + W_1 A + C_1^T C_1 & W_1 B_1 + C_1^T D_1 \\ B_1^T W_1 + D_1^T C_1 & D_1^T D_1 \end{bmatrix}. \tag{42}$$

With the help of the definition in (42) we can express the inequality in (41) as follows:

$$\begin{bmatrix} I & C^T K_{sof}^T \end{bmatrix} M(W_1) \begin{bmatrix} I \\ K_{sof} C \end{bmatrix} < 0. \tag{43}$$

It is possible to apply the elimination lemma to the above inequality. Elimination lemma states that if a symmetric matrix $Q_E \in \mathbb{R}^{n\times n}$ and matrices $B_E \in \mathbb{R}^{k\times n}$ and $C_E \in \mathbb{R}^{j\times n}$ be given then there exists a matrix $K_E \in \mathbb{R}^{j\times k}$ such that the set of inequalities

$$B_E^{\perp^T} Q_E B_E^{\perp} < 0 \text{ and } C_E^{\perp^T} Q_E C_E^{\perp} < 0 \tag{44}$$

is equivalent to the inequality

$$Q_E + C_E^T K_E B_E + B_E^T K_E^T C_E < 0. \tag{45}$$

In (45), $B_E^{\perp}$ and $C_E^{\perp}$ are the orthogonal complements of B_E and C_E, respectively.

Using the property of the elimination lemma described above, the inequality in (43) can be expressed as the inequality in (46) as follows:

$$M(W_1) + E_1 \begin{bmatrix} K_{sof} C & -I \end{bmatrix} + \begin{bmatrix} K_{sof} C & -I \end{bmatrix}^T E_1^T < 0. \tag{46}$$

The matrix E_1 is written in a block matrix form introducing two new variables F_s and F as follows:

$$E_1 = \begin{bmatrix} F_s \\ -F \end{bmatrix}. \tag{47}$$

Using (47), the inequality in (46) can now be written as follows:

$$M(W_1) + \begin{bmatrix} F_s K_{sof} C & -F_s \\ -F K_{sof} C & F \end{bmatrix} + \begin{bmatrix} C^T K_{sof}^T F_s^T & -C^T K_{sof}^T F^T \\ -F_s^T & F^T \end{bmatrix} < 0 . \tag{48}$$

By making use of the substitutions in (49) and (50) shown below:

$$F_s F^{-1} = K_{sf}^T \tag{49}$$

$$R = F K_{sof} \tag{50}$$

the inequality in (48) can be written as follows:

$$M(W_1)+\begin{bmatrix} K_{sf}^T RC & -K_{sf}^T F \\ -RC & F \end{bmatrix}+\begin{bmatrix} C^T R^T K_{sf} & -C^T R^T \\ -F^T K_{sf} & F^T \end{bmatrix}<0. \tag{51}$$

The above inequality has four optimization variables K_{sf}, R, W, and F. Since the matrix entries in the above inequality is nonlinear in these variables, an iterative procedure called the coordinate descent-type algorithm as described below is set up to solve the optimization problem [15].

a. Coordinate Descent-Type Algorithm [15]

1) A stable full-state feedback matrix K_{sf}^i forms the starting point of the algorithm.

2) Treating K_{sf}^i as a constant matrix, a convex optimization problem is setup with the objective of minimizing the H_2 norm $\|h(t)\|_2$ as defined in (39) subject to the LMI in (46). The matrices F and R corresponding to this optimal value (h_1) of $\|h(t)\|_2$ is kept constant.

3) With the above values of F and R the convex optimization problem of minimizing the H_2 norm is setup again treating K_{sf} and W as the optimization variables. The optimal value of the H_2 norm obtained in this step is equal to h_2.

4) The value of iteration i is increased. The optimal value of K_{sf} obtained in Step 3 forms the new K_{sf}^i to be used in Step 2. The iterations are repeated until a satisfactory value of $h_1 - h_2$ is obtained. When the iterations cease, the optimum values of R and K_{sof} are utilized to obtain the SOF controller by using the substitution in (47).

CHAPTER IV

CONTROLLER DESIGN AND RESULTS

A. Modeling

The first step in the design process is to model the system dynamics. In Figure 6, x_s and x_{us} are the sprung- and unsprung-mass displacements, respectively. F_{act} is the actuating force provided by the LBPMM. The spring stiffness k and the tire is modeled to have a stiffness of k_w and a damping coefficient of c_w. A friction force acts even on the sprung mass. In order to represent the quarter-car test bed as a linear system, this friction force is accounted for by introducing a damping coefficient c which acts only on the sprung mass. The free-body diagram in Figure 6 is used to generate the equations of motion.

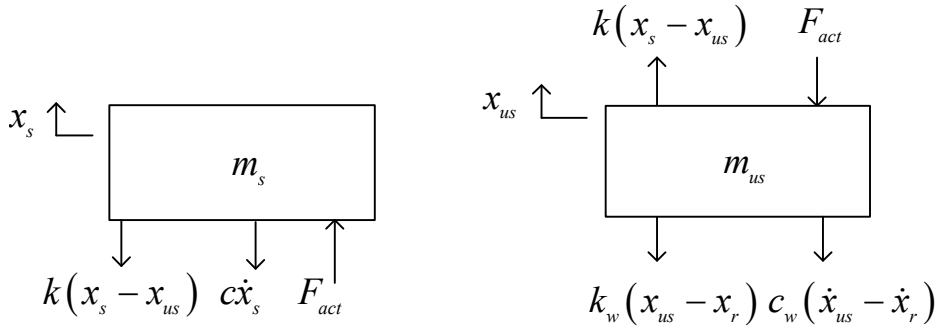

Figure 6. Free-body diagram of sprung and unsprung masses

The equations of motion derived from the free body diagram in Figure 2 are as follows:

$$m_s\ddot{x}_s = -k\left(x_s - x_{us}\right) - c\dot{x} + F_{act} \tag{52}$$

$$m_{us}\ddot{x}_{us} = k\left(x_s - x_{us}\right) - k_w\left(x_{us} - x_r\right) - c_w\left(\dot{x}_{us} - \dot{x}_r\right) - F_{act}. \tag{53}$$

The states of the quarter-car test bed are selected to be as follows:

$$[x_s \quad x_{us} \quad \dot{x}_s \quad \dot{x}_{us}]^T. \tag{54}$$

In terms of the states defined in (54), the quarter-car model can be represented as a state-space system defined in (2) as follows:

$$\begin{bmatrix} \dot{x}_s(t) \\ \dot{x}_{us}(t) \\ \ddot{x}_s(t) \\ \ddot{x}_{us}(t) \end{bmatrix} = \begin{bmatrix} 0 & 0 & 1 & 0 \\ 0 & 0 & 0 & 1 \\ -\dfrac{k}{m_s} & \dfrac{k}{m_s} & -\dfrac{c}{m_s} & 0 \\ \dfrac{k}{m_{us}} & -\dfrac{(k+k_w)}{m_{us}} & 0 & -\dfrac{c_w}{m_{us}} \end{bmatrix} \begin{bmatrix} x_s(t) \\ x_{us}(t) \\ \dot{x}_s(t) \\ \dot{x}_{us}(t) \end{bmatrix} + \begin{bmatrix} 0 & 0 \\ 0 & 0 \\ 0 & 0 \\ \dfrac{k_w}{m_{us}} & \dfrac{c_w}{m_{us}} \end{bmatrix} \begin{bmatrix} x_r(t) \\ \dot{x}_r(t) \end{bmatrix} + \begin{bmatrix} 0 \\ 0 \\ \dfrac{1}{m_s} \\ -\dfrac{1}{m_{us}} \end{bmatrix} F_{act}(t)$$

$$z_1 = \begin{bmatrix} -\dfrac{k}{m_s} & \dfrac{k}{m_s} & 0 & 0 \end{bmatrix} \begin{bmatrix} x_s(t) \\ x_{us}(t) \\ \dot{x}_s(t) \\ \dot{x}_{us}(t) \end{bmatrix} + \begin{bmatrix} \dfrac{1}{m_s} \end{bmatrix} F_{act}(t) \tag{55}$$

$$z_2 = \begin{bmatrix} 0 & 0 & 0 & 0 \end{bmatrix} \begin{bmatrix} x_s(t) \\ x_{us}(t) \\ \dot{x}_s(t) \\ \dot{x}_{us}(t) \end{bmatrix} + \begin{bmatrix} \dfrac{1}{F_{\max}} \end{bmatrix} F_{act}(t).$$

Once the dynamics of the system have been derived, it is required to find the parameters such as the sprung and unsprung masses, suspension spring stiffness, etc. which govern them. The values of the sprung and unsprung masses were measured to be

2.80 kg and 2.28 kg, respectively. In order to determine the value of the spring stiffness k, additional masses on the sprung mass were placed and the deflections of the spring from the mean position were noted. Figure 7 shows the corresponding data points. We see that up to a displacement of around 1.5 cm, the displacement is directly proportional to the added masses. By using the Hooke's law in this region, the spring stiffness k was then determined to be 840 N/m. The values of the damping coefficients c , c_w and the tire stiffness k_w shown in Table I in Chapter II, Subsection D were estimated through a process of trials and errors such that there was a good match between experiment and simulation.

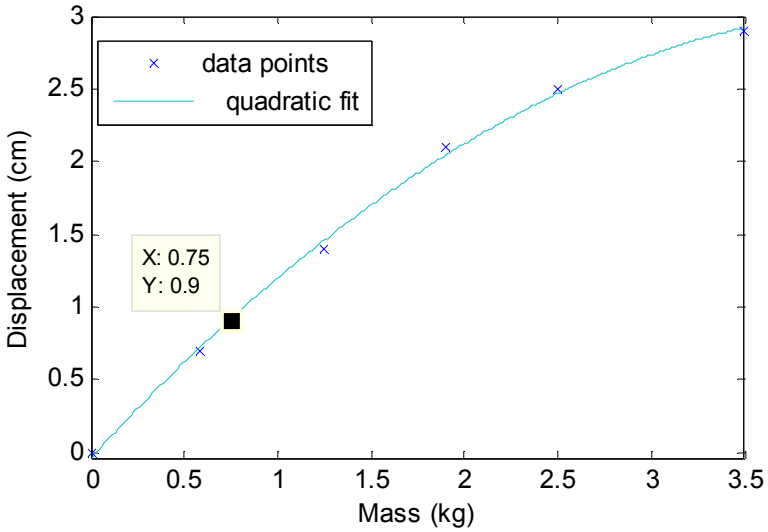

Figure 7. Deflection of suspension spring with added sprung mass

Figures 8 and 9 show the sprung and unsprung mass velocities respectively, when a road disturbance in the form of a sinusoid with a frequency of 2.2 Hz was applied in simulation and experiment. The figures show a good match between

simulation and experiment indicating a good estimation of the system parameters. A jerking action occurs when the tire passes through the top position of the cam. The effect of this action is greater on the unsprung mass as the stiffness of the tire is greater than that of the suspension spring. Hence a smooth profile of the unsprung-mass velocity is not obtained causing a discrepancy between experiment and simulation results.

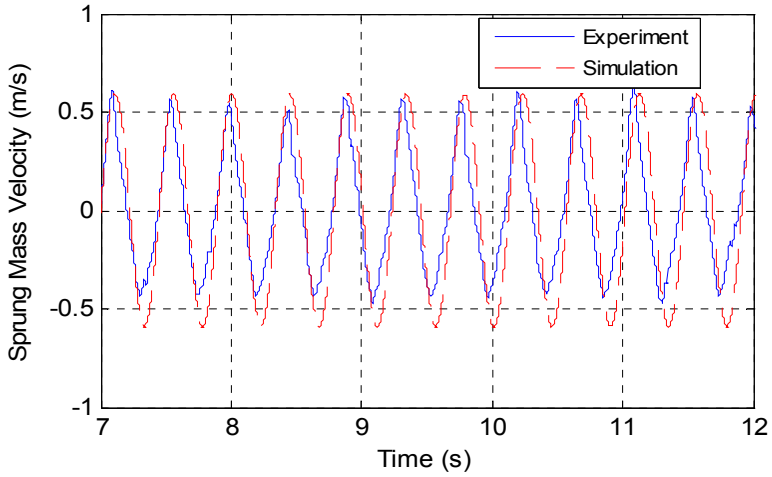

Figure 8. Sprung mass velocity in simulation and experiment (m_s = 2.8 kg; k = 840 N/m)

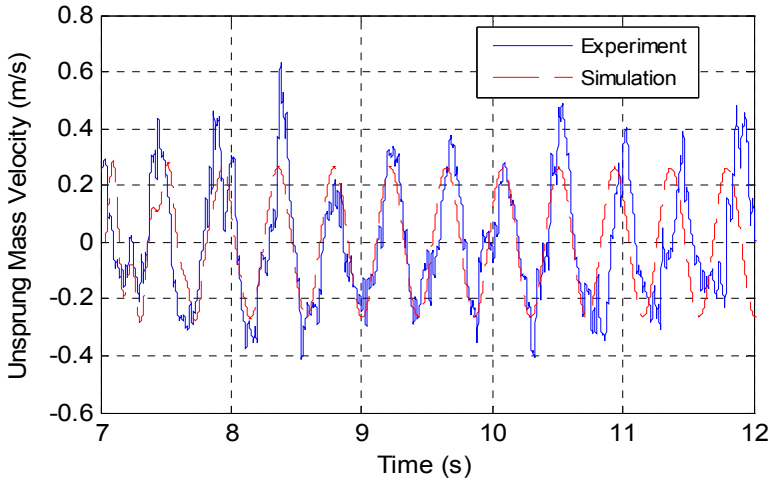

Figure 9. Unsprung mass velocity in simulation and experiment (m_s = 2.8 kg; k = 840 N/m)

B. Full-State Feedback Controller

Once the system is completely modeled and the system parameters are identified, it is now possible to design the control system. Following the steps provided in Chapter III of the thesis for the design of the FSF controller, the objectives of the control system are first defined. The primary objective is to minimize the $\|H\|_2$ from the input road disturbance to the sprung mass acceleration. The next objective is a performance constraint where the actuation force is to be limited to 25 N. Exceeding this force for a prolonged time may cause excess current to pass through the coils which might damage the magnets of the LBPMM.

Another constraint that can be added to the design of the control system is to force the poles to lie in a desired portion of the s - plane. This enables us to control certain performance characteristics such as damping ratios. In order to achieve this design specification, the dominant closed loop poles must lie in the shaded region of Figure 10 where the value of θ is as shown in (56) and ζ is the desired damping ratio expressed as follows:

$$\theta = \cos^{-1}(\zeta). \tag{56}$$

The LMI region corresponding to the shaded area in Figure 10 can be expressed as in (32) where the matrices N and M are as follows [7]:

$$N = \begin{bmatrix} 0 & 0 \\ 0 & 0 \end{bmatrix};\ M = \begin{bmatrix} \sin\theta & -\cos\theta \\ \cos\theta & \sin\theta \end{bmatrix}. \tag{57}$$

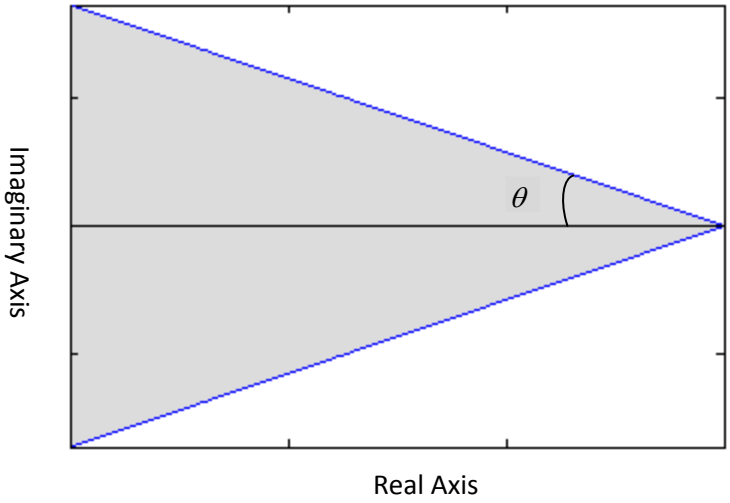

Figure 10. LMI region corresponding to a damping ratio of ζ

Once the control objectives have been identified they are cast as LMIs. The LMIs corresponding to the control objectives defined above are rewritten as follows:

$$\begin{bmatrix} AX + XA^T + B_u Y + Y^T B_u^T & B_1 \\ B_1^T & -I \end{bmatrix} < 0 \tag{58}$$

$$\begin{bmatrix} X & XC_1^T + XD_1^T \\ C_1 X + D_1 Y & Q \end{bmatrix} > 0 \; ; \; tr(Q) > \gamma \tag{59}$$

$$\begin{bmatrix} X & XC_2^T + Y^T D_2^T \\ C_2 X + D_2 Y & \nu I \end{bmatrix} > 0 \tag{60}$$

$$\left[n_{ij} X + m_{ij} (AX + B_u Y) + m_{ji} (XA^T + Y^T B_u^T) \right]_{ij} < 0. \tag{61}$$

The state-space matrices (defined in (2)) corresponding to the quarter-car model are obtained from (55). The matrices X, Y, and Q and the variable γ now need to be optimized such that the above inequality constraints are met and the value of γ is minimized. These variables must first be defined in order to solve the convex

optimization problem. For the case of the quarter-car model, X is a symmetric 4×4 matrix containing 10 variables, Y is a 1×4 matrix containing 4 variables and Q is a 1×1 matrix. Hence along with γ a total of 16 variables are present.

In order to completely define the LMIs, we must assign values to ν and ζ . The value of ν determines the limit on the actuating effort when a unit energy disturbance enters the system. In order to reduce conservativeness, a good knowledge of the road disturbance is essential. In the case of the quarter-car test bed the road disturbance can be modeled as

$$w = 0.015\sin(2.5t). \tag{62}$$

Even with the knowledge of the road disturbance, the only way the value of ν can be selected is to design the controller starting with an arbitrary value and checking the actuating effort applied in simulation when the road disturbance described in (62) is applied to the model. The greater the value of ν, the greater is the actuating effort applied. After trials and errors, a value of 520,000 was selected. This corresponds to a maximum actuating effort of 13 N when the road disturbance in (62) is applied in simulation. Although, a maximum force of 25 N can be applied, a smaller value of 13 N was chosen in simulation to account for the modeling uncertainties.

In order to satisfy the LMI given in (61) all the dominant and non-dominant poles must lie in the LMI region shown in Figure 10. Hence, it is not possible to constrain the location of selective poles. With many values of ζ tested, it was observed that increasing the damping ratio also increased the $\|H\|_2$. Hence, a small value of 0.2

was selected for ζ. Corresponding to these values of ζ, the matrices N and M were computed using (57) and are shown below:

$$N = \begin{bmatrix} 0 & 0 \\ 0 & 0 \end{bmatrix};\ M = \begin{bmatrix} 0.9798 & -0.2 \\ 0.2 & 0.9798 \end{bmatrix}. \tag{63}$$

Using the values of the matrices N and M in (64), the LMI in (62) is written as follows:

$$\begin{bmatrix} 0.9798(AX + B_u Y) + 0.9798(XA^T + Y^T B_u^T) & -0.2(AX + B_u Y) + 0.2(XA^T + Y^T B_u^T) \\ 0.2(AX + B_u Y) - 0.2(XA^T + Y^T B_u^T) & 0.9798(AX + B_u Y) + 0.9798(XA^T + Y^T B_u^T) \end{bmatrix} < 0. \tag{64}$$

Once the LMI variables and inequalities are defined, the convex optimization program B.1 in Appendix B is run with the help of the LMI control toolbox in MATLAB [6]. After optimization, the values of γ and the matrices X and Y were found to be as shown in (65), (66) and (67):

$$X = 1 \times 10^5 \begin{bmatrix} 0.0002 & 0 & -0.0008 & -0.0048 \\ 0 & 0.0013 & 0.0054 & -0.0083 \\ -0.0008 & 0.0054 & 0.0457 & -0.1019 \\ -0.0048 & -0.0083 & -0.1019 & 4.4647 \end{bmatrix} \tag{65}$$

$$Y = 1 \times 10^6 \begin{bmatrix} 0.0059 & -0.1269 & -0.7872 & 6.1578 \end{bmatrix} \tag{66}$$

$$\gamma = 2.166 \times 10^3 \text{ m/s}^2. \tag{67}$$

The full state feedback controller K_{sf} shown below is then obtained by using the substitution in (35):

$$K_{sf} = \begin{bmatrix} 803 & -809 & -1 & 23 \end{bmatrix}. \tag{68}$$

Thus this method was able to achieve a performance measure $\|H\|_2$ of $2.166 \times 10^3 \text{ m/s}^2$ corresponding to a generalized H_2 norm $\|H\|_g$ of the transfer function from z_2 to the

road disturbance of 293 N. The FSF controller obtained in (68) through the process of convex optimization is now tested on the quarter-car test bed. Due to the presence of a jerking action when the wheel moves on top of the cam, we see spikes in the acceleration of the sprung mass. Hence to give a better idea of the performance of the control system, we can also look at its effect on the velocity of the sprung mass. Since the magnitudes of the acceleration and velocity differ by a factor of ω, when the disturbance is in the form of a pure sinusoid of frequency ω, the percentage reduction in the acceleration of the sprung mass is equal to its percentage reduction in the velocity.

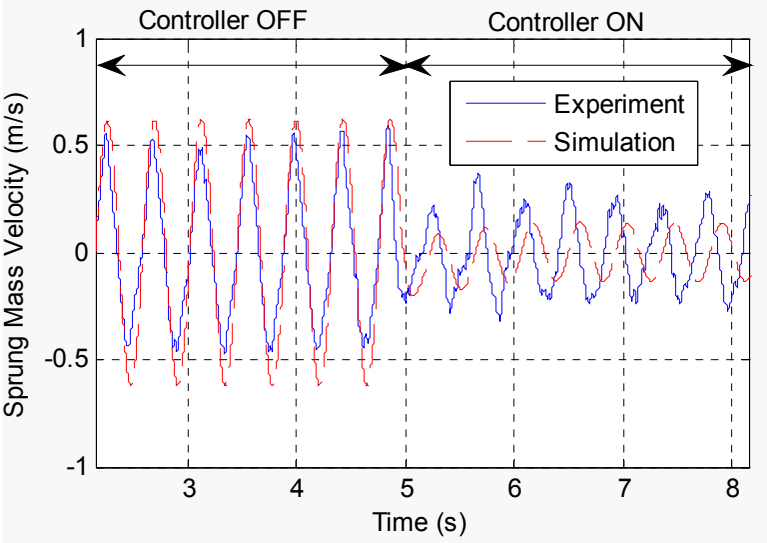

Figure 11. Sprung-mass velocity in experiment and simulation for full-state feedback ($m_s = 2.8$ kg; $k = 840$ N/m)

Figure 11 shows the sprung mass velocity in simulation and experiment, with the controller in the on and off positions when a sinusoidal input disturbance of frequency 2.3 Hz was applied to the system. From the figure, significant reduction in the peak-to-

peak velocity of the sprung mass can be observed along with a good match between the simulation and experimental results.

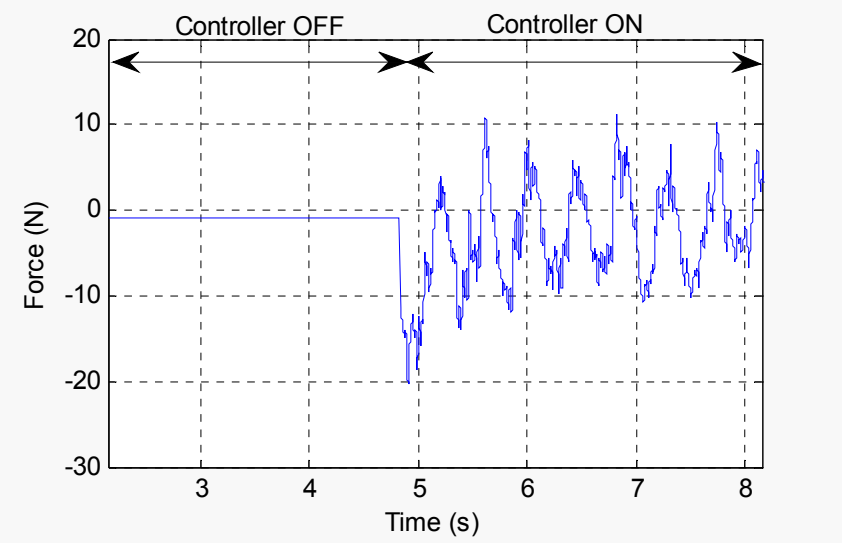

Figure 12. Actuating force calculated by the full-state feedback controller in experiment ($m_s = 2.8$ kg; $k = 840$ N/m)

The control force calculated by the full-state feedback controller during the experiment is shown in Figure 12. No current passes through the actuator when the controller is off. The non-zero offset when the controller is off It can be seen that the force does not exceed the saturation limit of 25 N, thus satisfying one of the control objectives. Figure 13 shows the currents passing through the three phases of the LBPMM during the experimental run. It can be seen that none of the three-phase currents passing through the LBPMM exceed 6 A. Figure 14 shows the location of the closed-loop poles of the quarter-car test bed with the full-state feedback control which are equal to the eigen values of the matrix A_{cl} . The values obtained were

$-8.325 \pm j38.615$ and $-2.367 \pm j2.605$. It is evident from the figure that none of the poles lie in the right hand plane, hence the system is stable. The poles also lie in the LMI region corresponding to a damping ratio of $\zeta = 0.2$. Although all the control objectives were satisfied, the full potential of the FSF controller could not be achieved as the data from the unsprung-mass accelerometer was not accurate due to the jerking motion experienced by the unsprung mass. In order to solve this problem where the data from the unsprung-mass accelerometer was not reliable, an SOF controller is designed based on the algorithm in [15].

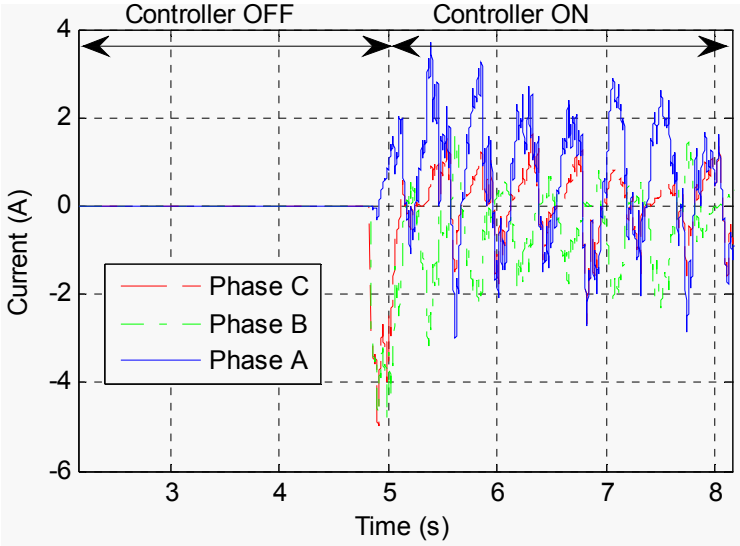

Figure 13. Current flow of the full-state feedback control in experiment ($m_s = 2.8$ kg; $k = 840$ N/m)

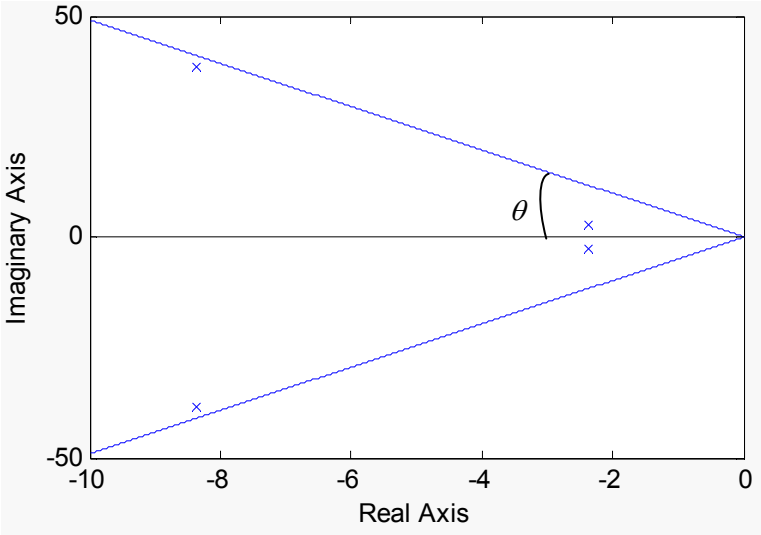

Figure 14. Position of the closed-loop poles for full-state feedback control

C. Static Output Feedback Controller

In order to design the SOF controller the procedure described in Chapter III is adopted. First, the linear matrix variable function $M(W_1)$ is defined as in (42) using the state space matrices corresponding to the quarter-car model in (55). Once, this function has been defined the LMI as expressed in (48) can be defined in order to run the coordinate-descent algorithm described in Chapter III. This LMI is rewritten in (69) as follows:

$$M(W_1)+\begin{bmatrix} K_{sfi}^T RC & -K_{sf}^T F \\ -RC & F \end{bmatrix}+\begin{bmatrix} C^T R^T K_{sfi} & -C^T R^T \\ -F^T K_{sfi} & F^T \end{bmatrix}<0. \tag{69}$$

It can be seen from the above inequality that the matrices K_{sfi}, R, F, and W_1 are the variables that need to be optimized such that it not only minimizes the value of the trace of the matrix $B_1^T W_1 B_1$ but also satisfies the inequality constraint in (69). The terms of

the matrices in the inequality in (69) which contain the products of the variables are nonlinear. Since each term of the matrices in the inequality must be affine in order to run the convex optimization problem, it is run in two parts. In the first part, the matrices R, F, and W_1 are treated as variables. For the quarter-car model, W_1 is a 4×4 positive definite symmetric matrix containing 10 variable elements, R is a 1×2 matrix containing 2 variable elements and F is a 1×1 matrix. The full-state feedback controller K_{sf} is taken as K_{sfi} in the first iteration of the coordinate-descent algorithm.

In the second part of the algorithm the matrices K_{sfi} and W_1 form the variables. The matrix K_{sfi} is defined as a 1×4 matrix containing 4 variables. The optimum values of R and F obtained as a result of running the convex optimization program in the first part of the algorithm are used in the second part. The optimization program is run again to get new values K_{sfi} and W_1. Several iterations of the algorithm are run until the value of the trace of the matrix $B_1^T W_1 B_1$ in successive iterations does not differ by more than a desired value λ. The program to run this algorithm is written in the LMI toolbox of MATLAB and shown in Appendix B.2 where the value of λ is taken to be 10. The values of the matrices R, F, and W_1 obtained at the end of the iterations are shown below:

$$R = \begin{bmatrix} -204.5 & 130.0 \end{bmatrix};\ F = -0.14 \tag{70}$$

$$W_1 = \begin{bmatrix} 105.3 & -4.2 & 3.7 & 0.1 \\ -4.2 & 492.4 & -149.6 & 1.0 \\ 3.7 & -149.6 & 92.0 & -0.6 \\ 0.1 & 1.0 & -0.6 & 0.2 \end{bmatrix}. \tag{71}$$

Making use of the substitution in (50) the following SOF controller K_{sof} is obtained:

$$K_{sof} = [1420.6 \quad -903.0]. \tag{72}$$

Figure 15 shows the exerted actuating force when the SOF controller designed above is used in simulation when the input road disturbance is equal to that in (62). The figure clearly shows that the actuating effort would exceed the allowable value of 25 N in simulation. Also while performing the experiment, the controller is turned on after the cam reaches the desired frequency of rotation (around 2.5 Hz). As a result, because of the large gains the initial control effort would be very large as is evident from the spike in the magnitude of force in Figure 15. Hence, this controller cannot be implemented to the experimental setup. In order to solve the above problem, a multi-objective coordinate-descent algorithm [15] is used. In order to achieve this multi-objective control, it is required that the inequalities expressed in (28) and (31) (which ensure that the performance output z_2 does not exceed a certain value equal to the square root of ν when a unit energy disturbance is the input into the system) be expressed in the form of the LMI in (48).

The inequalities (28) and (31) when expanded in terms of the SOF control matrix K_{sof} and the state-space matrices in (2), we obtain the following inequalities:

$$(A + B_u K_{sof} C)W_2 + W_2(A^T + C^T K_{sof}^T B_u^T) + B_1 B_1^T < 0$$

$$\Rightarrow \begin{bmatrix} I & B_u K_{sof} C \end{bmatrix} M(W_2) \begin{bmatrix} I \\ C^T K_{sof}^T B_u^T \end{bmatrix} < 0 \tag{73}$$

$$P_3 - \frac{1}{\nu}(C_2 + D_2 K_{sof} C)^T (C_2 + D_2 K_{sof} C) > 0$$

$$\Rightarrow \begin{bmatrix} I & C^T K_{sof}^T \end{bmatrix} M(W_3) \begin{bmatrix} I \\ K_{sof} C \end{bmatrix} > 0 \tag{74}$$

where $M(W_2) = \begin{bmatrix} AW_2 + W_2 A^T + B_1 B_1^T & W_2 \\ W_2 & 0 \end{bmatrix}$ and $M(W_3) = \begin{bmatrix} W_3 - \frac{1}{\nu} C_2^T C_2 & -\frac{1}{\nu} C_2^T D_2 \\ -\frac{1}{\nu} D_2^T C_2 & -\frac{1}{\nu} D_2^T D_2 \end{bmatrix}$.

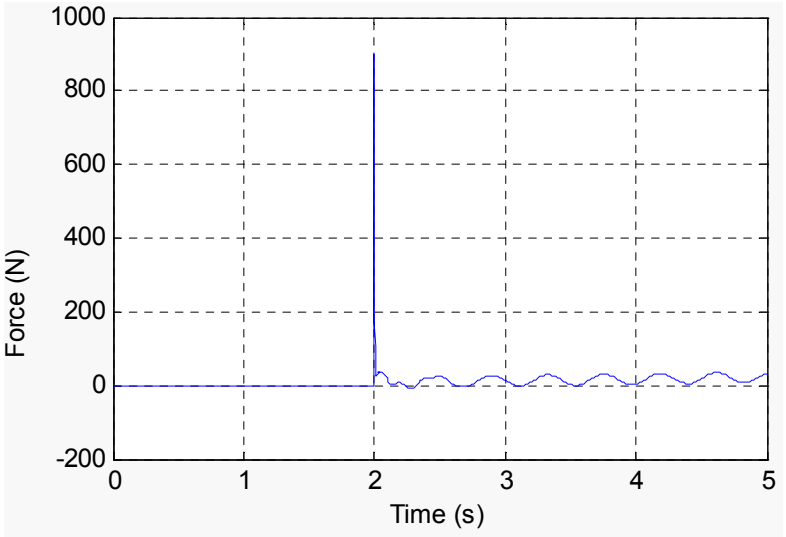

Figure 15. Control effort in simulation without constraint using SOF control ($m_s = 2.8$ kg; $k = 840$ N/m))

Applying the elimination lemma to (73)—(74), we obtain the following inequalities:

$$M(W_2) + E_2\begin{bmatrix} C^T K_{sof}^T B_u^T & -I \end{bmatrix} + \begin{bmatrix} I \\ B_u K_{sof} C \end{bmatrix} E_2 < 0 \tag{75}$$

$$M(W_3) + E_3\begin{bmatrix} K_{sof} C & -I \end{bmatrix} + \begin{bmatrix} C' K_{sof}^T \\ -I \end{bmatrix} E_3^T < 0. \tag{76}$$

We see that although the inequalities in (48), (75), and (76) are of the similar form, the coordinate-descent algorithm cannot be applied because of the nonlinear constraint $W_2 = W_3^{-1}$. Hence the method of introducing slack variables by applying the elimination lemma in the case of multi-objective control leads us to the initial problem of nonlinearity we tried to solve.

In order to solve this problem, we make use of the fact that for a single-input, single-output system, the generalized H_2 norm as described in (13) is equivalent to the following equation [24]:

$$\|H\|_g = \inf_{P_4} \{ \left\| B_1^T W_4 B_1 \right\|^{\frac{1}{2}} : W_4 A_{cl} + A_{cl}^T W_4 + C_{cl2}^T C_{cl2} < 0 \}. \tag{77}$$

Following the same procedure as above (introducing slack variables by applying elimination lemma) we obtain the inequality

$$M(W_4) + E_4\begin{bmatrix} KC & -I \end{bmatrix} + \begin{bmatrix} C^T K^T \\ -I \end{bmatrix} E_4' < 0 \tag{78}$$

where $M(W_4) = \begin{bmatrix} A^T W_4 + W_4 A + C_2^T C_2 & W_4 B_1 + C_2^T D_2 \\ B_1^T P_4 + D_2^T C_2 & D_2^T D_2 \end{bmatrix}$. By equating W_4 and W_1, and E_4 and E_1 the coordinate descent algorithm can be run which seeks to minimize both the H_2 norm of the transfer function $H(s)$ and also the generalized H_2 norm $\|H\|_g$ of the

transfer function from the road disturbance to the control effort. However equating W_4 and W_1 would mean that both the norms would be forced to be equal. Hence a weighing factor α is introduced on the constrained output z_2 (control effort). The coordinate descent algorithm is now run to minimize $\|H\|_2$ satisfying the inequality constraints of (48) and (78) for different values of α .

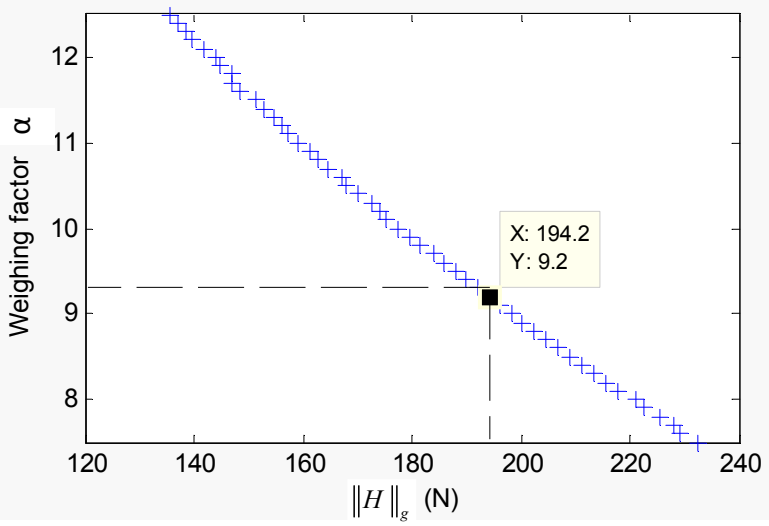

Figure 16. Value of generalized H_2 norm $\|H\|_g$ of the transfer function from control effort to road disturbance for various values of α .

Figure 16 shows the value of $\|H\|_g$ for different values of α . We see that the effect of the inverse of α is similar to the effect of ν in the full-state feedback control design. The greater is the value of α , the smaller is the available control effort. The value of α was so chosen by some trials and errors such that the control effort in simulation did not exceed 14 N. This resulted in a value of $\|H\|_g$ equal to 194.2 N.

The coordinate-descent algorithm is run with the value of $\alpha = 9.2$. The optimum value of the matrices R, F, and W_1 obtained for this value of α are shown in (79) and (80) as follows:

$$R = \begin{bmatrix} -67.9 & 27.8 \end{bmatrix}; \; F = -0.268 \tag{79}$$

$$W_1 = W_4 = \begin{bmatrix} 8757.0 & 443.5 & 117.3 & 7.4 \\ 443.5 & 4368.9 & 49.7 & 16.9 \\ 117.3 & 49.7 & 44.3 & 1.2 \\ 7.4 & 16.9 & 1.2 & 2.6 \end{bmatrix}. \tag{80}$$

Making use of the substitution in (50) the SOF controller K_{sof} shown in (81) is obtained as follows:

$$K_{sof} = \begin{bmatrix} 254 & -103.8 \end{bmatrix} \tag{81}$$

giving a value of 1707.7 m/s^2 for the H_2 norm of $H(s)$.

Figure 17 shows the effect of the SOF controller in simulation and experiment. We see that there is a very good match between the experimental and simulation results and the sprung-mass velocity is considerably attenuated when the controller is turned on. When the controller is turned off, we see that the magnitude of the sprung-mass velocity is smaller in the downward direction in experiment. When running the simulation it was assumed that the spring stiffness remains constant and is independent of its deflection. However, the physical spring that we have exhibits variable stiffness as is seen in Figure 7. Hence, when the spring is compressed (i.e, when the sprung mass is below its equilibrium position) its stiffness increases and the sprung mass is unable to reach the

expected velocity. As a result the sprung mass velocity in experiment is less than that in simulation in the downward direction when the controller is turned off.

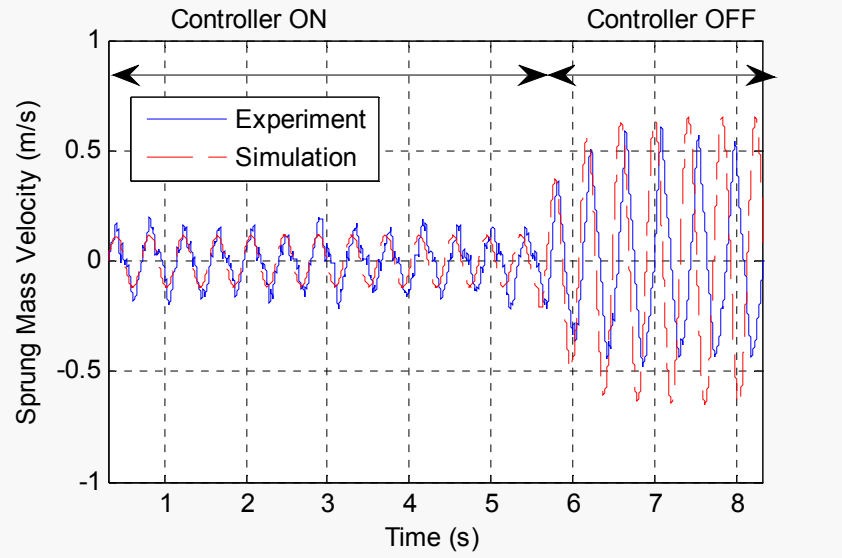

Figure 17. Sprung-mass velocity in experiment and simulation for the SOF control ($m_s = 2.8$ kg; $k = 840$ N/m)

Figure 18 shows the control force calculated by the SOF controller in experiment. It is evident from the figure that the control objective of restricting the control force to less that 25 N is successful. Figure 19 shows the current passing through the three coils of the LBPMM. We see that the current in the three phase coils does not exceed 6 A. When the controller is off no current is passed through the actuator.

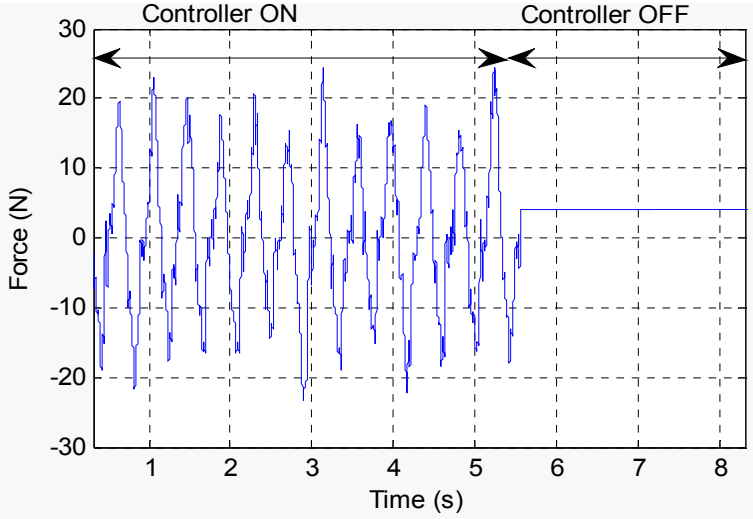

Figure 18. Control force calculated by SOF controller in experiment
(m_s = 2.8 kg; k = 840 N/m)

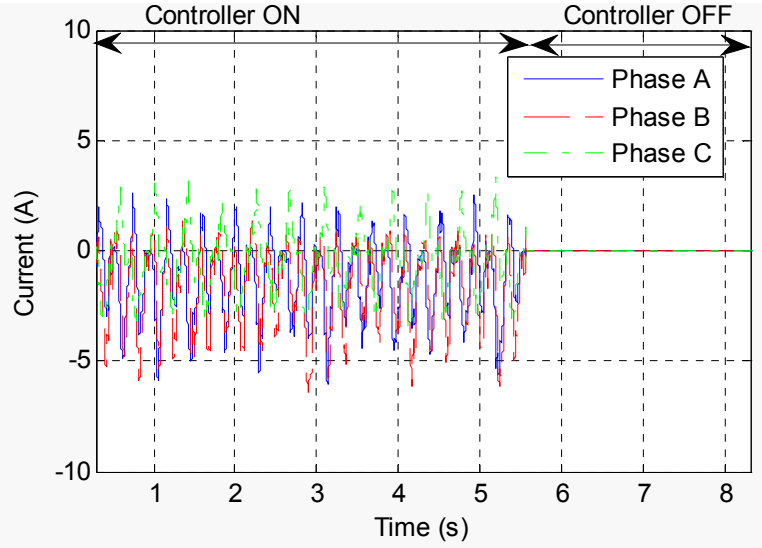

Figure 19. Current in the three phase coils of the LBPMM for SOF control
(m_s = 2.8 kg; k = 840 N/m)

The above controller was designed for a particular value of sprung mass. When the loading and unloading of a vehicle causes significant change in the value of the

sprung mass, it may be desirable to have a control system which changes to accommodate the variation in the sprung mass. In order to achieve this, the SOF controller is designed for incrementing values of sprung mass. The value of α corresponding to each value of sprung mass is chosen such that the generalized H_2 norm $\|H\|_g$ remains constant. This process can be automated by designing the full-state feedback and SOF controllers using the method described in Chapter III for various values of sprung mass incremented through an iterative procedure. In this thesis the controller is designed for three of these values of the sprung mass (2.3kg, 2.8kg, and 3.4kg). If we represent the two elements of the SOF control matrix as follows:

$$K_{sof} = \begin{bmatrix} Ks_1 & Ks_2 \end{bmatrix}. \tag{82}$$

then Figure 20 shows how these elements change with respect to the sprung mass. The figures were obtained by running the convex optimization program given in Program B.3 in Appendix B. Through this program, for each value of the sprung mass the FSF control matrix K_{sf} is computed which is used in computing the SOF control matrix K_{sof}. A quadratic curve is fitted over these data points. If a vehicle has an online sensor measuring the value of the sprung mass, the process of designing a control system specific to each value can be automated. In Figure 20 the circular data points correspond to the three values of the sprung mass (2.3 kg, 2.8 kg, and 3.4 kg) for which the SOF control was tested on the quarter-car test bed. The effect of applying the SOF controller on the quarter-car test bed with sprung mass values of 2.3 kg and 3.4 kg is shown in Appendix A.1 and A.2, respectively. If the value of the sprung mass is increased beyond

3.4 kg, it results in excessive compression of the suspension spring. Hence the SOF controller could not be tested with a heavier sprung mass in our current test bed.

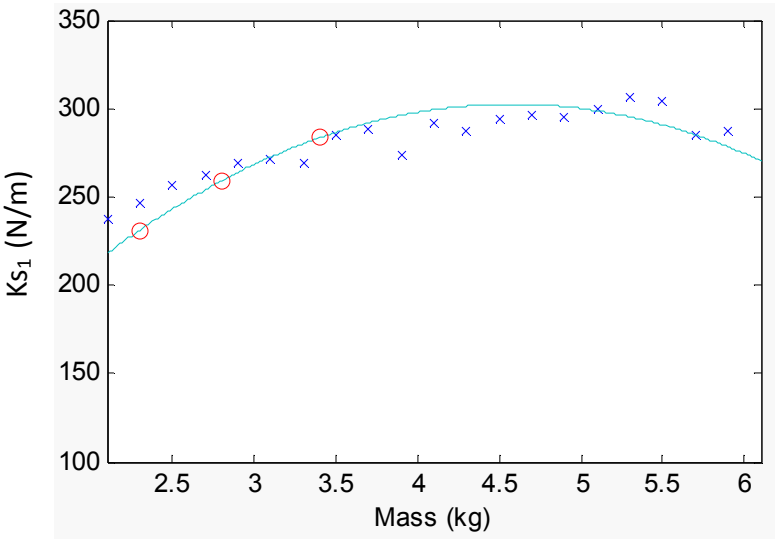

Figure 20(a). Ks_1 vs sprung mass fitted with a quadratic curve

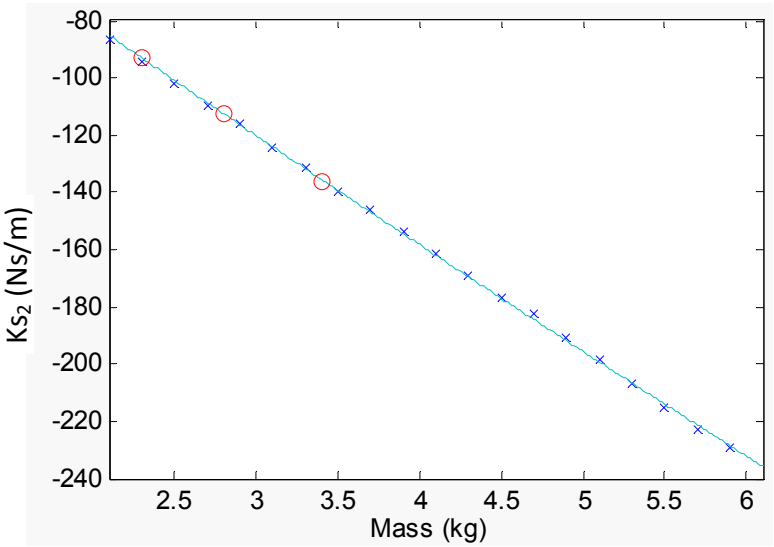

Figure 20(b). Ks_2 vs sprung mass fitted with a quadratic curve

The sprung mass value is then kept constant at 3.4 kg and a new suspension spring with a stiffness of 1640 N/m is used. The SOF controller is now designed for the new set of parameters such that the value of $\|H\|_g$ remains 195 N. The optimum values of the variables R, F, and W_1 obtained are shown in (83) and (84) as follows:

$$R = \begin{bmatrix} -32.7 & 11.5 \end{bmatrix}; \; F = -0.2005 \tag{83}$$

$$W_1 = W_4 = \begin{bmatrix} 1217.9 & -3140 & 170 & -36 \\ -3140 & 13622 & -41 & 43 \\ 170 & -41 & 40 & 3 \\ -36 & 43 & 3 & 7 \end{bmatrix}. \tag{84}$$

The SOF control gain matrix K_{sof} obtained is as follows:

$$K_{sof} = \begin{bmatrix} 163 & -57 \end{bmatrix}. \tag{85}$$

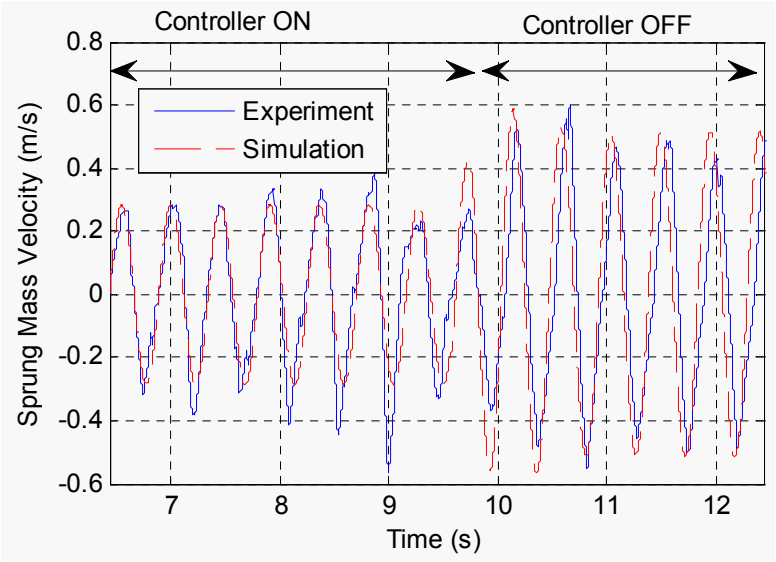

Figure 21. Sprung-mass velocity in experiment and simulation for SOF control ($m_s = 3.4$ kg; $k = 1640$ N/ m)

The effect of this SOF controller in simulation and experiment is shown in Figure 21. When a suspension spring with greater stiffness is used, a greater value of control effort would be required to achieve a similar attenuation in the sprung-mass velocity. Since the maximum force exerted by the LBPMM is 25 N, we see that the attenuation of the sprung-mass velocity is less when the stiffness of the suspension spring increases. Figure 22 shows the force exerted by the LBPMM in experiment. The control objective of limiting the actuating force to less that 25 N is satisfied for most part of this experimental run.

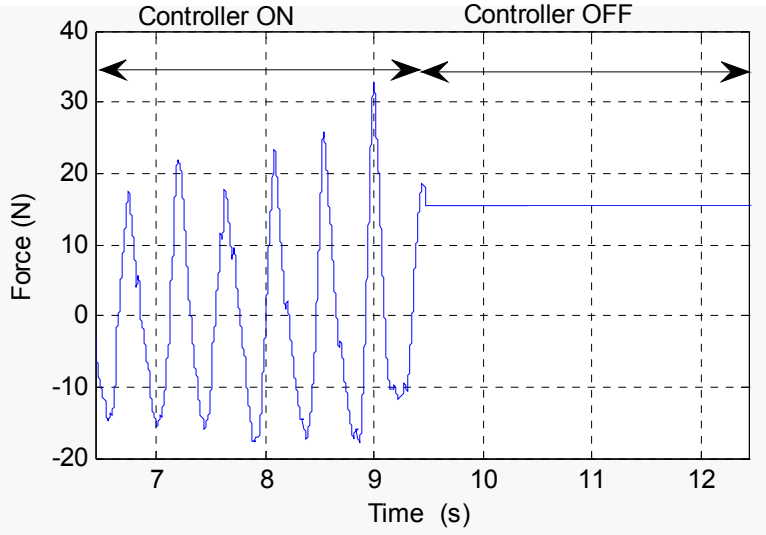

Figure 22. Control force calculated by SOF controller in experiment ($m_s = 3.4$ kg; $k = 1640$ N/ m)

D. Modified Lead-Lag Controller

Using the parameters of the quarter-car model in Table I, the transfer function $G(s)$ from the actuating force F_{act} to the sprung mass velocity $\dot{x}_s$ is as shown in (86):

$$G(s) = \frac{0.3704s^3 + 2.4388s^2 + 569s + 4.07\times10^{-10}}{s^4 + 12.88s^3 + 2258s^2 + 4.404\times10^4 s + 4.78\times10^5}. \quad (86)$$

The first step in the design of the lead-lag controller is to obtain the behavior of the system in the frequency domain. This information is obtained with the help of a Bode plot of $G(s)$. Figure 23 shows the Bode plot of $G(s)$ (sys1) with the parameters in Table I and the Bode plot shown (sys2) with the parameters used by Lee [3]. Since both the profiles are similar, the control system designed by Lee can be used with minor modifications. The compensator is to be designed such that the loop transfer function has a bandwidth between 10 rad/s and 80 rad/s which corresponds to the vibrations to which the human body is most susceptible [3].

A lag controller was introduced at low frequencies to adjust the crossover frequency to obtain the desired bandwidth. Another lag controller was introduced at high frequencies to attenuate the noise. Finally in order to increase the gain and phase margins in the desired bandwidth to allow for modeling uncertainties a lead controller was introduced. The MATLAB SISOTOOLS was used to adjust the compensator design for the new values of the quarter-car parameters. The compensator shown in (87) as follows:

$$C(s) = 515.69\frac{(1+0.00047s)(1+0.019s)(1+0.19s)}{(1+0.003s)(1+0.011s)(1+s)} \quad (87)$$

is finally used.

Figure 24 shows the Bode plot of the loop transfer function $C(s)G(s)$ (compensated system) and of the open-loop transfer function $G(s)$ (uncompensated

system). A bandwidth between 4 rad/s and 80 rad/s is achieved with a gain of about 60 dB in this region.

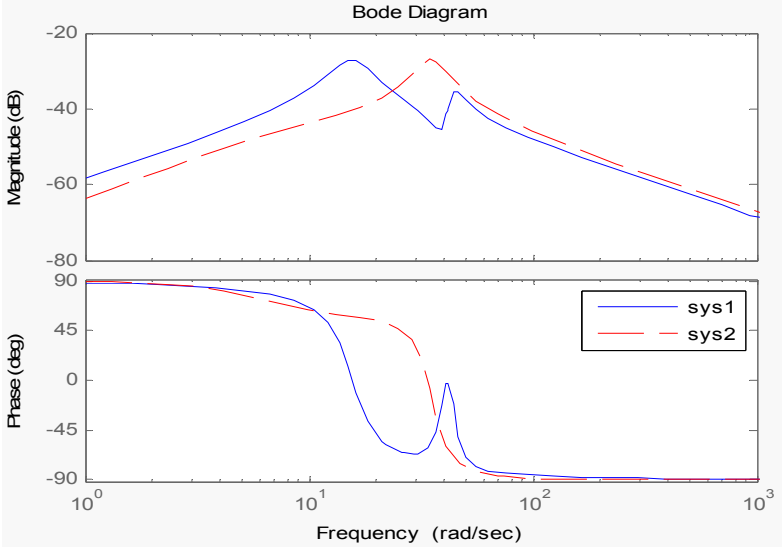

Figure 23. Bode plot of the transfer function from F_{act} to $\dot{x}_s$ with quarter-car model parameters from Table I (sys1) and that from Lee [3] (sys2)

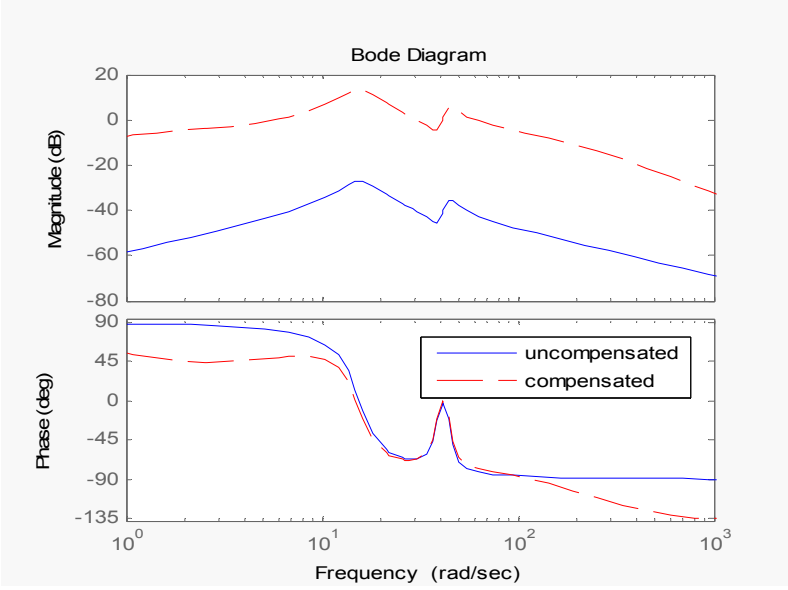

Figure 24. Bode plot of the compensated and uncompensated loop transfer function

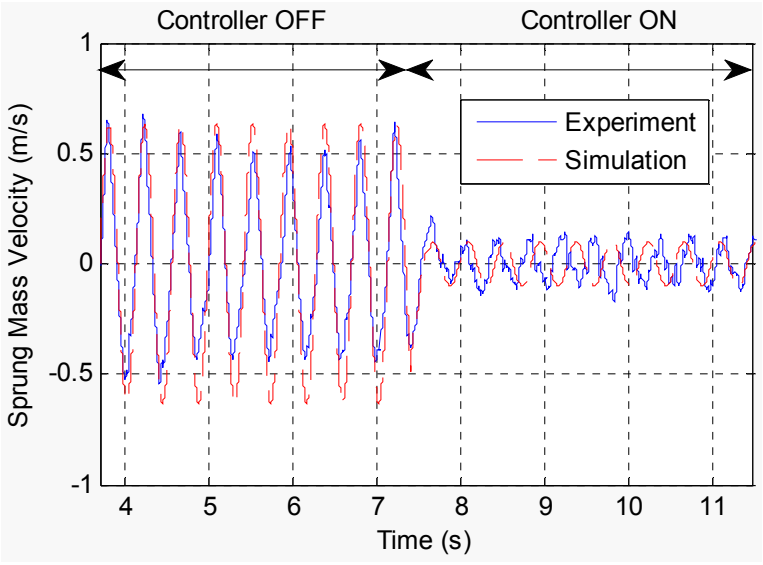

Figure 25. Sprung-mass velocity with modified lead-lag compensator in experiment and simulation ($m_s = 2.8$ kg; $k = 840$ N/m)

The modified lead-lag compensator was then applied on the quarter-car test bed. Figure 25 gives a comparison of the sprung mass velocity in simulation and experiment with the controller ON and OFF. We see a significant attenuation of the sprung mass velocity and a good agreement between experiment and simulation. The modified lead-lag compensator is also applied to the sprung mass values corresponding to 2.3 kg and 3.4 kg. The results of applying the modified lead-lag compensator on the quarter-car test bed for these values of sprung mass are provided in Appendix A.3 and A.4, respectively.

CHAPTER V

PERFORMANCE ANALYSIS

In this subsection, a performance comparison of the SOF controller with the modified lead-lag compensator is made. Several trials were conducted by applying the two types of controllers on the quarter-car test bed. The best performance achieved in each case is used for the analysis in this subsection.

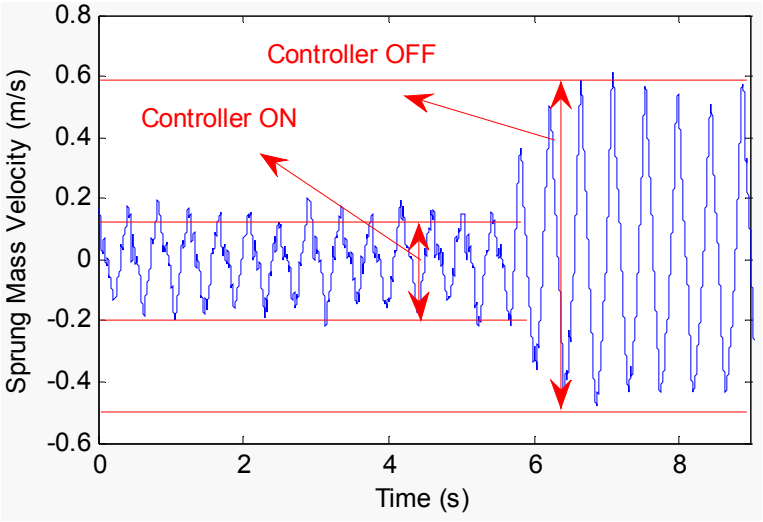

Figure 26. Performance of the SOF controller ($m_s = 2.8$ kg; $k = 840$ N/m)

As stated in Chapter IV, when the disturbance is purely sinusoidal, the percentage reduction in acceleration of the sprung mass would be equal to the percentage reduction of its velocity. As a measure of performance of the controller, the reduction in the peak-to-peak velocity is considered in this analysis as shown in (88):

$$Perf_{LMI} = \left(1 - \frac{LMI_{on}}{LMI_{off}}\right) \times 100 = 72\%. \tag{88}$$

Figure 26 shows the effect of the SOF controller on the sprung mass velocity. The peak-to-peak velocity with the SOF controller off (LMI_{off}) is 1.03 m/s and with controller on (LMI_{on}) is 0.29 m/s. A 72% reduction in the peak-to-peak velocity is obtained at a frequency of 2.4 Hz.

The similar performance criterion is now applied to the modified lead-lag controller. Figure 27 shows the result of applying the modified lead-lag compensator in experiment.

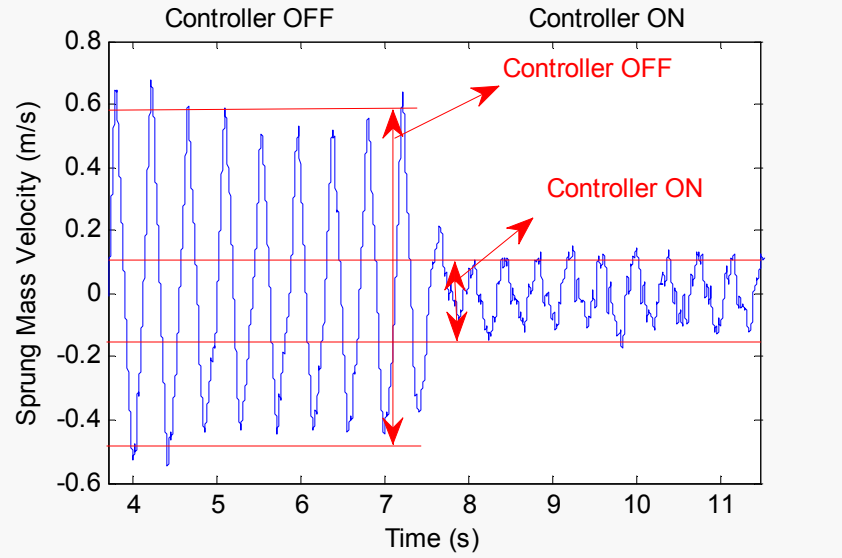

Figure 27. Performance of the modified lead-lag compensator ($m_s = 2.8$ kg; $k = 840$ N/m)

The peak-to-peak velocity with the controller is turned off ($leadlag_{off}$) is 1.03 m/s. The peak-to-peak velocity with the controller on ($leadlag_{on}$) is 0.24 m/s. A 77%

reduction in the peak-to-peak velocity is obtained at a frequency of 2.4 Hz as shown below:

$$Perf_{LMI} = \left(1 - \frac{leadlag_{on}}{leadlag_{off}}\right) \times 100 = 77\%. \tag{89}$$

We see that the modified lead-lag compensator performs slightly better than the SOF controller with the 2.4 Hz road disturbance.

A similar analysis on the effect of the SOF controller and the modified lead-lag compensator on the quarter car test bed with sprung mass of 2.3 kg and 3.4 kg are given in Appendix A.1 – A.4. Increasing the sprung mass beyond 3.4 kg causes an excessive compression of the suspension spring. Hence simulation results are provided for a sprung mass of 6.0 kg.

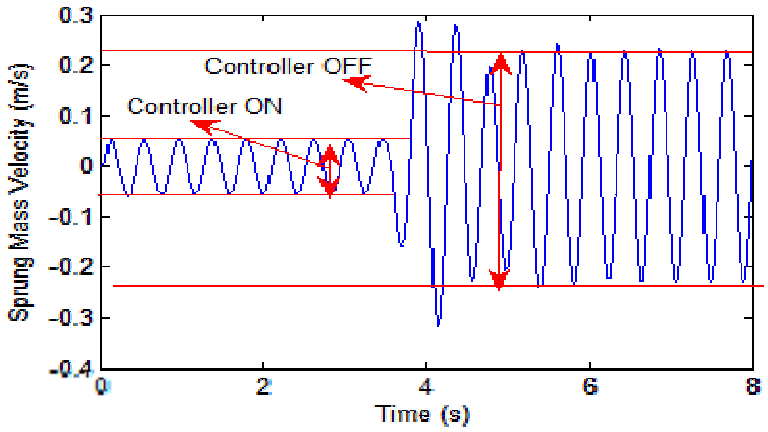

Figure 28. Performance of the SOF controller ($m_s = 2.8$ kg; $k = 840$ N/m) in simulation

From Figure 20, the SOF control gain matrix is obtained and is found to be [273 −238]. Figure 28 shows the effect of this controller on the quarter-car system in simulation. The peak-to-peak sprung mass velocities at 2.4 Hz frequency road

disturbance with the controller on and off is 0.11 m/s and 0.46m/s, respectively. An attenuation of 76% in the peak-to-peak velocity is obtained as shown below:

$$Perf_{LMI} = \left(1 - \frac{LMI_{on}}{LMI_{off}}\right) \times 100 = \left(1 - \frac{0.11}{0.46}\right) = 76\% \tag{90}$$

Figure 29 shows the effect of the modified lead-lag compensator on the quarter-car system in simulation. The peak-to-peak sprung mass velocities with the compensator on and off are 0.21 m/s and 0.46 m/s, respectively. An attenuation of 54% is achieved on the peak-to-peak velocity as shown below:

$$Perf_{LMI} = \left(1 - \frac{leadlag_{on}}{leadlag_{off}}\right) \times 100 = \left(1 - \frac{0.21}{0.46}\right) = 54\%. \tag{91}$$

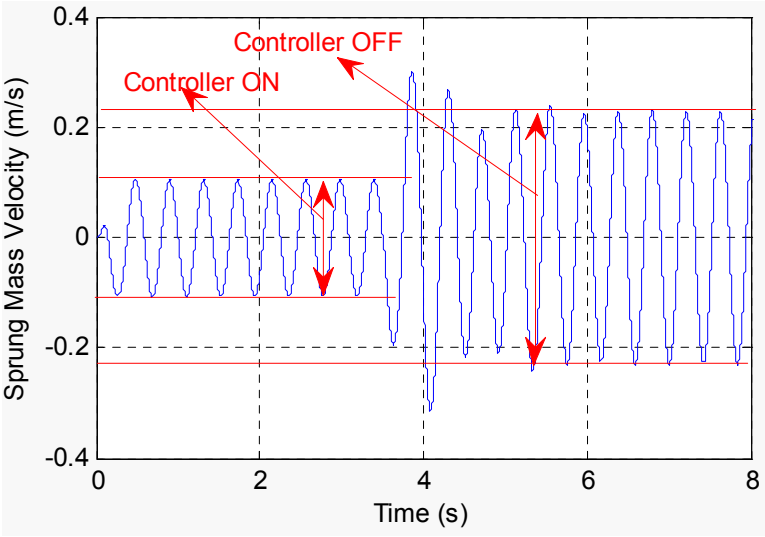

Figure 29. Performance of the modified lead-lag compensator (m_s = 6.0 kg; k = 840 N/m) in simulation

The reduction in the peak-to-peak velocity corresponding to the three values of sprung mass for which the SOF controller and the modified lead-lag compensator were tested and the simulation results corresponding to a sprung mass value of 6.0 kg are provided in Table II.

Table II

Percentage reduction in sprung-mass peak-to-peak velocity

Sprung mass (kg)	SOF controller	Modified lead-lag compensator
2.3	73	79
2.8	72	77
3.4	71	69
6.0	76	54

Keeping the sprung mass at 3.4 kg, the suspension spring stiffness is now changed to 1640 N/m. Figures 30 and 31 show the performance of the SOF and modified lead-lag compensator on the quarter-car test bed. The peak-to-peak sprung-mass velocity with the controller OFF is 0.98 m/s at a frequency of 2.2 Hz. The modified lead-lag compensator attenuated the peak-to-peak velocity to 0.43 m/s and the SOF controller attenuated the peak-to-peak velocity to 0.57 m/s. The percentage reduction in the peak-to-peak velocities for these cases is shown as follows:

$$Perf_{LMI} = \left(1 - \frac{LMI_{on}}{LMI_{off}}\right) \times 100 = \left(1 - \frac{0.57}{0.98}\right) = 42\% \tag{92}$$

$$Perf_{LMI} = \left(1 - \frac{leadlag_{on}}{leadlag_{off}}\right) \times 100 = \left(1 - \frac{0.43}{0.98}\right) = 54\%. \tag{93}$$

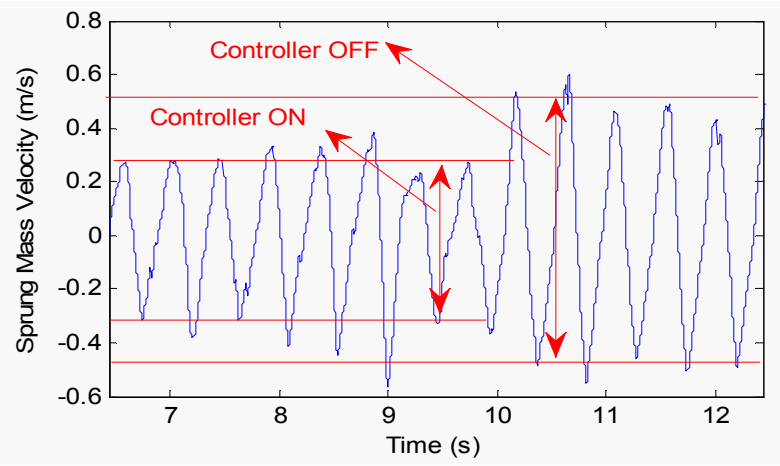

Figure 30. Performance of the SOF controller ($m_s = 3.4$; $k = 1640$ N/m)

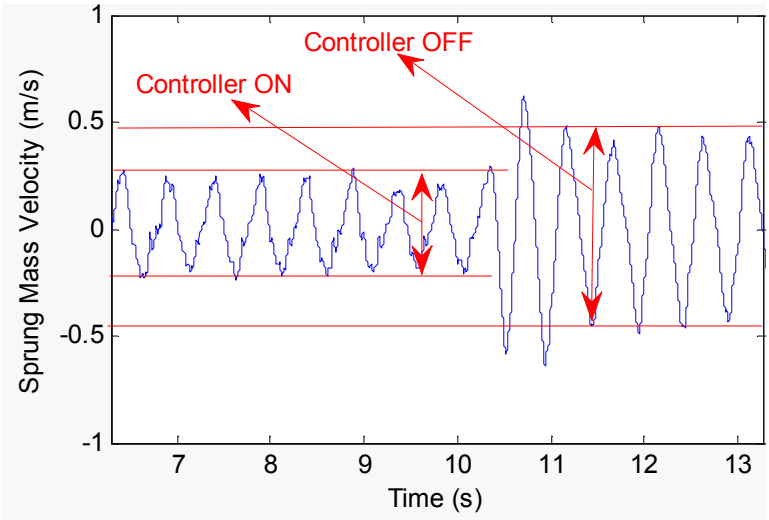

Figure 31. Performance of the modified lead-lag compensator ($m_s = 3.4$; $k = 1640$ N/m)

CHAPTER VI

CONCLUSIONS

The quarter-car test bed built by Allen [1] formed a platform for testing various control methodologies. Lee [3] designed four separate controllers using modified lead-lag, LQ servo with Kalman filter, fuzzy control and SMC and implemented them on the quarter-car test bed achieving a maximum attenuation of 78% on the peak-to-peak velocity of the sprung mass. This thesis aimed at testing numerical methods of control using convex optimization on the quarter-car test bed.

The parameters of the quarter-car test bed were first found through experiment and trials and errors. Once the governing dynamics were modeled, a full-state feedback controller was designed using convex optimization by expressing the control objectives of minimizing the H_2 norm and limiting the actuating effort as LMIs. An H_2 norm value of 2.166×10^3 m/s^2 for the transfer function from sprung mass acceleration to input road disturbance was obtained. The effectiveness of the controller was demonstrated in experiment and simulation.

The full potential of the full-state feedback controller could not be achieved as the data from the unsprung-mass accelerometer was not accurate because of a jerking motion experienced by the unsprung mass. In order to solve this problem, output feedback control methods were explored. The coordinate descent algorithm employed in [15] was selected to design an SOF controller. However, since the algorithm did not place any constraint on the amount of control effort available, very large control gains

were obtained. The algorithm was modified to constrain the amount of actuating effort available. The full-state feedback controller formed the starting point in the design of the SOF controller. The modified algorithm was then run to generate the SOF controller. An H_2 norm value of 1.707×10^3 m/s^2 was achieved. The algorithm was then run in a loop with increasing values of sprung mass in order to generate a profile which showed how the entries in the gain matrix of the SOF controller changed with changing mass. This process allows for the automation of control system design which can implement an SOF controller specific to a particular sprung mass.

The control method was validated by implementing the SOF controller on the quarter-car test bed for sprung-mass values of 2.3 kg, 2.8 kg and 3.4 kg. An attenuation of the peak-to-peak velocity of the sprung mass of 73%, 72% and 71% was achieved, respectively. For the same values of the sprung mass, the modified lead lag compensator achieved an attenuation of 79%, 77% and 69% respectively. For the sprung mass corresponding to 3.4 kg, the value of the suspension spring was then changed to 1640 N. The simulation results showed that the SOF controller was able to attenuate the peak-to-peak sprung mass velocity by 76% and the modified lead-lag compensator achieved an attenuation of 54%. The SOF controller was able to achieve a 42 % attenuation of the peak-to-peak sprung-mass velocity. The modified lead-lag compensator was able to attenuate the sprung-mass peak-to-peak velocity by 54%.

As demonstrated by the above figures, the SOF controller was able to achieve a comparable performance to that of the modified lead-lag controller in experiment. As shown by the simulation result, when the sprung mass is increased to 6.0 kg, the gain of

the modified lead-lag compensator has to be recomputed.to achieve a similar performance as that of the SOF controller.

The constraints of the quarter-car test bed did not allow testing the controllers for a greater range of sprung mass and spring stiffness values. Increasing the sprung mass caused excessive compression of the suspension spring. Also, the increased load increased the torque on the cam shaft powered by the drill. As a result the rotation of the cam was not smooth. The maximum force exerted by the LBPMM is 25 N. This did not allow for a stiffer suspension spring to be used.

One of the significant advantages of the SOF controller is that it minimizes the need for trial and error and design intuition associated with classical control design. Also, since the SOF controller does not require the use of an estimator it is very easy to implement. Future work in this area would consist of improving the test bed to allow for the controllers to be tested on a greater range of sprung mass and spring stiffness values.

REFERENCES

[1] J. Allen, "Design of active suspension control based upon tubular linear motor and quarter-car model,*"* Master's thesis, Texas A&M Univ. College Station, TX, 2008.

[2] B. C. Murphy, "Design and construction of a precision tubular linear motor and controller*," Master's* thesis, Texas A&M Univ. College Station, TX, 2003.

[3] S. Lee, "Active suspension control with direct-drive tubular linear permanent-magnet motor*," Master's* thesis, Texas A&M Univ. College Station, TX, 2009.

[4] S. Boyd, L. El Ghaoui, E. Feron, and V. Balakishnan, *Linear Matrix Inequalities in System and Control Theory*. Philadelphia: SIAM, 1994.

[5] Y. Nesterov and A. Nemirovsky, *Interior-Point Polynomial Methods in Convex Programming*. Philadelphia: SIAM, 1994.

[6] P. Gahinet, A. Nemirovski, A. Laub, and M. Chilali, "The LMI control toolbox," in Proc. Of *IEEE Conference on Decision and Control, December 1994, Florida, U.S.A,* pp. 2038–2041.

[7] M. Chilali and P. Gahinet, "H_∞ design with pole placement constraints: An LMI approach", *IEEE Trans. on Automatic Control*, vol. 41, no. 3, pp. 358–367, March 1996.

[8] I. Masubuchi, N. Suda, and A. Ohara, "LMI-based controller synthesis: A unified formulation and solution," *International Journal of Robust and Nonlinear Control,* vol. 8, no. 8, pp. 669–686, July 1998.

[9] C. W. Scherer, P. Gahinet, and M. Cbilali, "Multi-objective output-feedback control via LMI optimization," *IEEE Trans. Automatic Control*, vol. 42, no. 7, pp. 896–911, January 1997.

[10] V. L. Syrmos, C. T. Abdallah, P. Dorato, and K. Grigoriadis, "Static output feedback – A survey," *Automatica,* vol. 33, no. 2, pp. 125–137, February 1997.

[11] J. C. Geromel, P. L. D. Peres, and S. R. Souza, "Convex analysis of output feedback control problems: Robust stability and performance," *IEEE Trans. Automatic Control*, vol. 41, no. 7, pp. 997–1003, July 1996.

[12] M. C. de Oliveira and J. C. Geromel, "Numerical comparison of output feedback design methods," in *Proc. 1997 American Control Conference,* June 1997, vol. 1, no. 4, pp. 72–76.

[13] J. V. Burke, D. Henrion, A. S. Lewis, and M. L. Overton, "Stabilization via nonsmooth, nonconvex optimization," *IEEE Trans. Automatic Control,* vol. 51, no. 11, pp. 1760–1769, November 2006.

[14] J. Gumussoy, P. Millstone, and M. L. Overton, " H_∞ strong stabilization via HIFOO, a package for fixed-order controller design," in Proc. Of *IEEE Conference on Decision and Control, January 2009, Cancun, Mexico,* pp. 4135–4140.

[15] D. Peaucelle and D. Arzelier, "An efficient numerical solution for H_2 static output feedback synthesis," in *Proc. Of European Control Conference*, September 2001, Porto, Portugal, pp. 3800–3805.

[16] W. S. Levine and M. Athans, "On the determination of the optimal constant output feedback gains for linear multivariable systems," *IEEE Trans. Automatic Control,* vol. 15, no. 1, pp. 44–48, February 1970.

[17] P. M. Makila and H. T. Toivonen, "Computational methods for parametric LQ problems – A survey," *IEEE Trans. Automatic Control,* vol. 32, no. 8, pp. 658–671, August 1987.

[18] J. C. Geromel, C. C. de Souza, and R. E. Skelton, "Static output feedback controllers: Stability and convexity," *IEEE Trans. Automatic Control,* vol. 43, no. 1, pp. 120–125, January 1998.

[19] L. El Ghaoui, F. Oustry, and M. Aitrami, "A cone complementarity linearization algorithm for static output-feedback and related problems," *IEEE Trans. Automatic Control,* vol. 42, no. 8, pp. 1171–1176, August 1997.

[20] D. Arzelier, E. N. Gryazina, D. Peaucelle, and B. T. Polyak, "Mixed LMI/randomized methods for static output feedback control design," in *Proceedings of American Control Conference*, July 2010, Baltimore, Maryland, pp. 4683–4688.

[21] B. T. Polyak and E. N Gryazina, "Hit-and-Run: new design technique for stabilization, robustness and optimization of linear systems," in *Proceedings of IFAC World Congress, July 2008, Seoul, South Korea,* pp. 376 –380.

[22] H. Chen, P. Y. Sun, and K. H. Guo, "A multi-objective control design for active suspensions with hard constraints," in *Proc. of the American Control Conference 1,* November 2003, pp. 4371–4376.

[23] H. Gao, P. Lam, and K. Wang, "Multi-objective control of vehicle suspension systems via load-dependent controllers," *Journal of Sound and Vibrations,* vol. 290, no. 3–5, pp. 654–675, March 2006.

[24] R. E. Skelton, T. Iwasaki, and K. Grigoriadis. *A Unified Algebraic Approach to Linear Control Design.* PA: Taylor Francis, 1997.

APPENDIX A

EXPERIMENTAL RESULTS

A.1 Performance of SOF controller with sprung mass = 2.3 kg

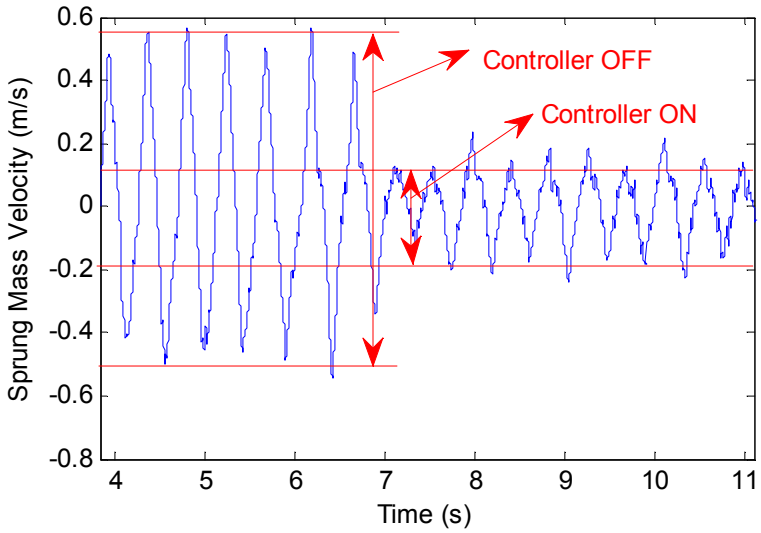

$$Perf_{LMI} = \left(1 - \frac{LMI_{on}}{LMI_{off}}\right) \times 100 = \left(1 - \frac{0.28}{1.02}\right) = 73\%$$

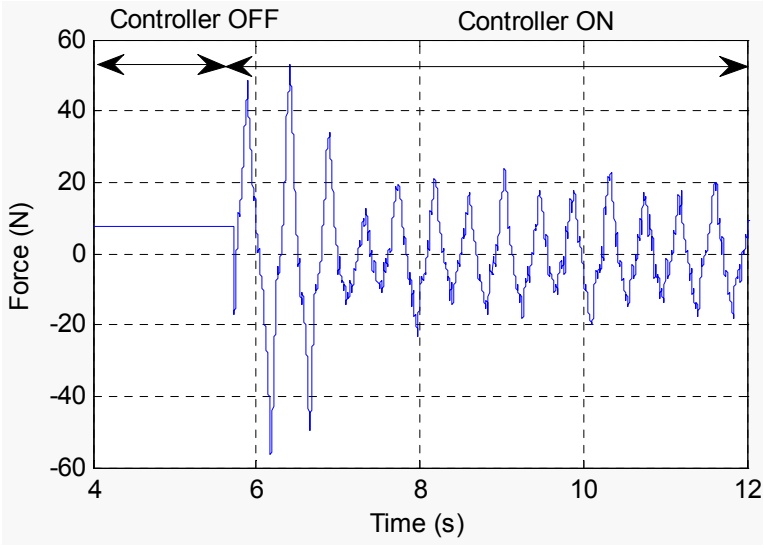

A.2 Performance of SOF controller with sprung mass = 3.4 kg

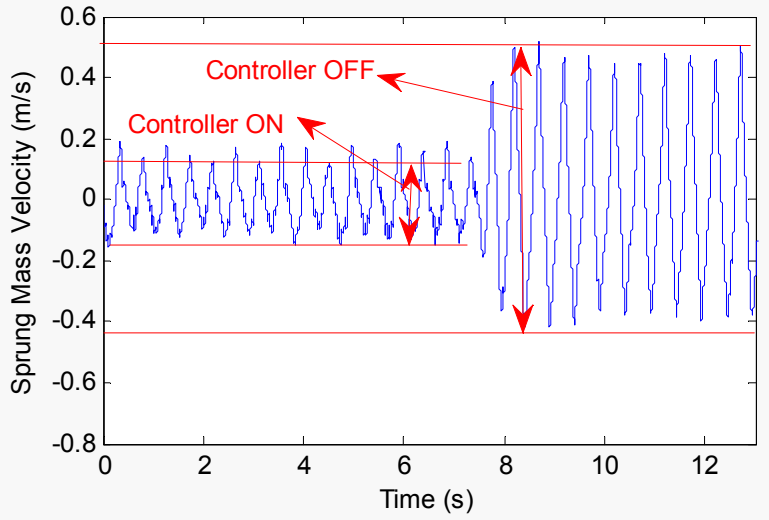

$$Perf_{LMI} = \left(1 - \frac{LMI_{on}}{LMI_{off}}\right) \times 100 = \left(1 - \frac{0.25}{0.90}\right) = 71\%$$

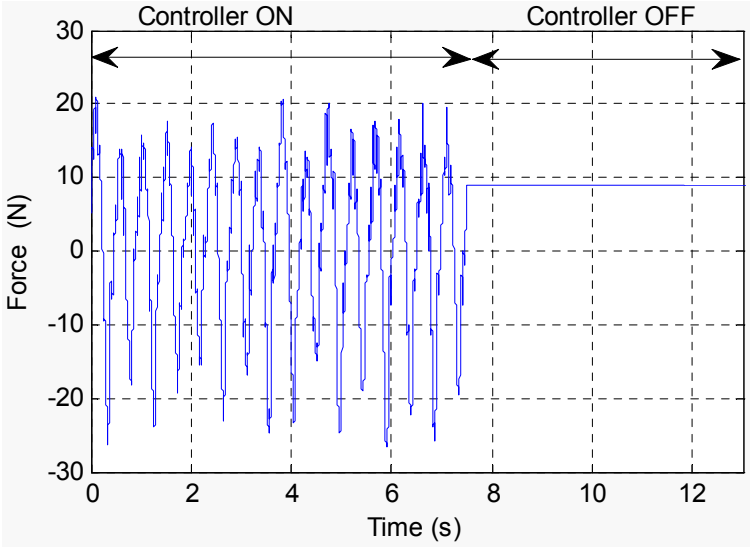

A.3 Performance of modified lead-lag controller with sprung mass = 2.3 kg

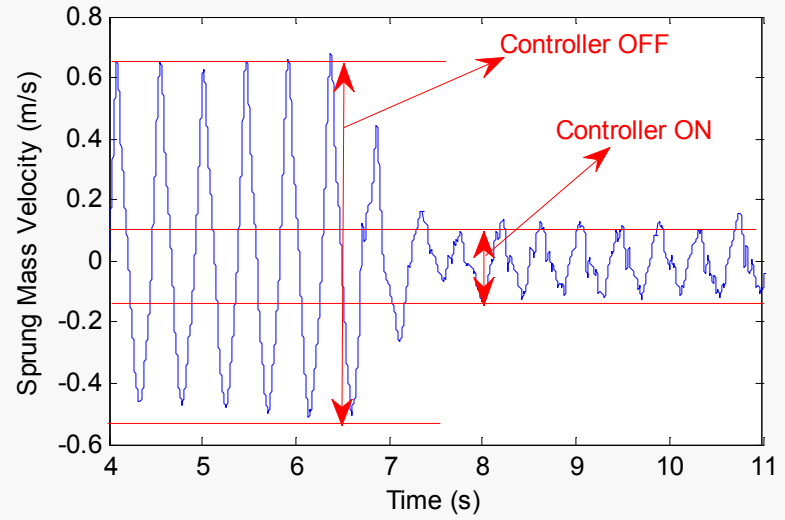

$$Perf_{LMI} = \left(1 - \frac{lead - lag_{on}}{lead - lag_{off}}\right) \times 100 = \left(1 - \frac{0.23}{1.12}\right) = 79\%$$

A.4 Performance of modified lead-lag controller with sprung mass = 3.4 kg

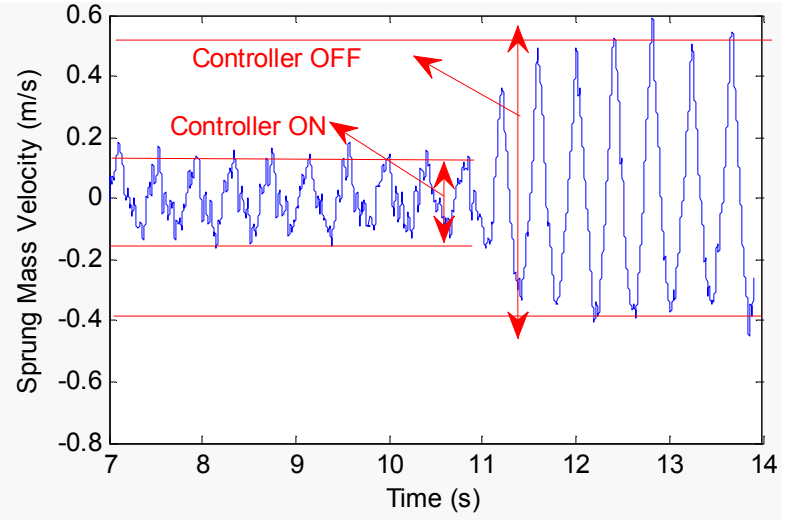

$$Perf_{LMI} = \left(1 - \frac{lead - lag_{on}}{lead - lag_{off}}\right) \times 100 = \left(1 - \frac{0.28}{0.91}\right) = 69\%$$

APPENDIX B

LMI PROGRAMS IN MATLAB

B.1 Program to generate the full-state output feedback controller

```
clc
ms=2.8;
mus=2.278;
k=840;
kw=3500;
c=17;
cw=15;
A=[0 0 1 0; 0 0 0 1; -k/ms k/ms -c/ms 0; k/mus -(k+kw)/mus 0 -cw/mus];
B1=[0; 0; 0; kw/mus];
B2=[0;0;0;cw/mus];
Bu=[0; 0; 1/ms; -1/mus];
B=[B1 B2 Bu];
Bw=[B1 B2];
C1=[-k/ms k/ms -c/ms 0 ];
C2=[0 0 0 0];
Cc=[1 0 0 0; 0 0 1 0];
D1u=1/ms;
D2u=1/(25);
setlmis([]);
Q= lmivar(1,[4 1]);
Y= lmivar(2,[1 4]);
S= lmivar(1,[1 1]);
U2= lmivar(1,[1 1]);
h1=newlmi;
lmiterm([h1 1 1 Q],A,1,'s');
lmiterm([h1 1 1 Y],Bu,1,'s');
lmiterm([h1 2 1 0],Bw');
lmiterm([h1 2 2 0],-1);
h2= newlmi;
lmiterm([-h2 1 1 Q],1,1);
lmiterm([-h2 2 1 Y],D1u,1);
lmiterm([-h2 2 1 Q],C1,1);
lmiterm([-h2 2 2 S],1,1);
h3=newlmi;
lmiterm([h3 1 1 S],1,1);
lmiterm([-h3 1 1 U2],1,1);
h4=newlmi;
lmiterm([-h4 1 1 Q],1,1);
lmiterm([-h4 2 1 Q],C2,1);
lmiterm([-h4 2 1 Y],D2u,1);
lmiterm([-h4 2 2 0],280000);
ndecv=decnbr(lmis)
c=[0 0 0 0 0 0 0 0 0 0 0 0 0 0 0 1];
[copt,xopt]=mincx(lmis,c)
yopt=dec2mat(lmis,xopt,2)
qopt=dec2mat(lmis,xopt,1)
```

```
K=yopt*inv(qopt)
Acl=A+Bu*K;
Ccl=C1+D1u*K;
syscl1=ss(Acl,Bw,Ccl,0);
Wc=gram(syscl1,'c');
h2=sqrt(Ccl*Wc*Ccl')
Ccl2=C2+D2u*K;
syscl2=ss(Acl,Bw,Ccl2,0);
Wc2=gram(syscl2,'c');
h23=sqrt(Ccl2*Wc2*Ccl2')
```

B.2 Program to generate the static output feedback controller starting with the full-state feedback controller

```
clc
ms=2.8;
mus=2.278;
k=840;
kw=3500;
cw=15;
c=17;
A=[0 0 1 0; 0 0 0 1; -k/ms k/ms -c/ms 0; k/mus -(k+kw)/mus 0 -cw/mus];
Br=[0; 0; 0; kw/mus];
Bv=[0;0;0;cw/mus];
B=[0; 0; 1/ms; -1/mus];
B2=[Br Bv];
C2=[-k/ms k/ms c/ms 0 ];
C=[1 0 0 0; 0 0 1 0];
C3=[0 0 0 0] ;
alpha=7;
while(alpha<12)
s=alpha
D3=alpha*1/25;
D2=1/ms;
v=100;
i=1;
Ks1=[809 -815 -1 23];
while (i<10)
    if(i>1)
    Ksi=Ks2;
    else
    Ksi=Ks1;
    end
setlmis([]);
P= lmivar(1,[4 1]);
R= lmivar(2,[2 1]);
F= lmivar(1,[1 1]);
h1= newlmi;
lmiterm([h1 1 1 P],A',1,'s');
lmiterm([h1 1 1 R],C',Ksi,'s');
```

```
lmiterm([h1 1 1 0],C2'*C2);
lmiterm([h1 1 2 P],1,B);
lmiterm([h1 1 2 R],-C',1);
lmiterm([h1 1 2 F],-Ksi',1);
lmiterm([h1 1 2 0],C2'*D2);
lmiterm([h1 2 2 F],1,1,'s');
lmiterm([h1 2 2 0],D2'*D2);
h2=newlmi;
lmiterm([-h2 1 1 P],1,1);
h3=newlmi;
lmiterm([h3 1 1 P],A',1,'s');
lmiterm([h3 1 1 R],C',Ksi,'s');
lmiterm([h3 1 2 P],1,B);
lmiterm([h3 1 2 F],-Ksi',1);
lmiterm([h3 1 2 R],-C',1);
lmiterm([h3 2 2 F],1,1,'s');
lmiterm([h3 2 2 0],D3'*D3);
lmis=getlmis;
n=decnbr(lmis);
c=zeros(n,1);
 for j=1:n
    [Pj,Rj,Fj]=defcx(lmis,j,P,R,F);
    c(j)=trace(Br'*Pj*Br)+trace(Bv'*Pj*Bv);
end
c;
[copt1,xopt]=mincx(lmis,c);
copt1;
Ropt=dec2mat(lmis,xopt,2);
Fopt=dec2mat(lmis,xopt,3);
Kopt=inv(Fopt)*Ropt'
xopt;
setlmis([]);
P=lmivar(1,[4,1]);
Ks=lmivar(2,[1 4]);
h4=newlmi;
lmiterm([h4 1 1 P],A',1,'s');
lmiterm([h4 1 1 Ks],C'*Ropt,1,'s');
lmiterm([h4 1 1 0],C2'*C2);
lmiterm([h4 1 2 P], 1,B);
lmiterm([h4 1 2 -Ks], 1, -Fopt);
lmiterm([h4 1 2 0], C2'*D2-C'*Ropt);
lmiterm([h4 2 2 0 ], D2'*D2+Fopt+Fopt');
h5=newlmi;
lmiterm([h5 1 1 P],A',1,'s');
lmiterm([h5 1 1 Ks],C'*Ropt,1,'s');
lmiterm([h5 1 2 P], 1,B);
lmiterm([h5 1 2 -Ks], 1, -Fopt);
lmiterm([h5 1 2 0], -C'*Ropt);
lmiterm([h5 2 2 0 ], D3'*D3+Fopt+Fopt');
h6=newlmi;
lmiterm([-h6 1 1 P],1,1);
newlmis=getlmis;
n=decnbr(newlmis)
c=zeros(n,1);
```

```
for j=1:n
    [Pj,Ksj]=defcx(newlmis,j,P,Ks);
    c(j)=trace(Br'*Pj*Br)+trace(Bv'*Pj*Bv);
end
[copt2,xopt]=mincx( newlmis,c);
copt2;
Ks2=dec2mat(newlmis,xopt,2);
v=copt1-copt2;
i=i+1;
end
Ccl3=D3/alpha*Kopt*C;
Acl=A+B*Kopt*C;
Ccl=C2+D2*Kopt*C;
sys=ss(Acl,B2,Ccl,0);
sys3=ss(Acl,B2,Ccl3,0);
Wc=gram(sys,'c');
Wc3=gram(sys3,'c');
h2=sqrt(Ccl*Wc*Ccl');
h23=sqrt(Ccl3*Wc3*Ccl3');
figure(3)
plot(h23,alpha,'+');
hold on
alpha=alpha+0.1;
end
```

B.3 Program to generate the profile of the matrix entries of the sof controller for different values of sprung mass

```
clc
ms=2.8;
p=1;
x=zeros(1,22);
y=zeros(1,22);
m=zeros(1,22);
while(ms<6.5)
mus=2.278;
k=840;
kw=3500;
c=17;
cw=15;
A=[0 0 1 0; 0 0 0 1; -k/ms k/ms -c/ms 0; k/mus -(k+kw)/mus 0 -cw/mus];
B1=[0; 0; 0; kw/mus];
B2=[0;0;0;cw/mus];
Bu=[0; 0; 1/ms; -1/mus];
B=[B1 B2 Bu];
Bw=[B1 B2];
C1=[-k/ms k/ms -c/ms 0 ];
C2=[0 0 0 0];
C=[1 0 0 0; 0 0 1 0];
D1u=1/ms;
D2u=1/(25);
```

```
setlmis([]);
Q= lmivar(1,[4 1]);
Y= lmivar(2,[1 4]);
S= lmivar(1,[1 1]);
U2= lmivar(1,[1 1]);
h1=newlmi;
lmiterm([h1 1 1 Q],A,1,'s');
lmiterm([h1 1 1 Y],Bu,1,'s');
lmiterm([h1 2 1 0],Bw');
lmiterm([h1 2 2 0],-1);
h2= newlmi;
lmiterm([-h2 1 1 Q],1,1);
lmiterm([-h2 2 1 Y],D1u,1);
lmiterm([-h2 2 1 Q],C1,1);
lmiterm([-h2 2 2 S],1,1);
h3=newlmi;
lmiterm([h3 1 1 S],1,1);
lmiterm([-h3 1 1 U2],1,1);
h4=newlmi;
lmiterm([-h4 1 1 Q],1,1);
lmiterm([-h4 2 1 Q],C2,1);
lmiterm([-h4 2 1 Y],D2u,1);
lmiterm([-h4 2 2 0],180000);
lmis=getlmis;
ndecv=decnbr(lmis);
c=[0 0 0 0 0 0 0 0 0 0 0 0 0 0 0 1];
[copt,xopt]=mincx(lmis,c);
yopt=dec2mat(lmis,xopt,2);
qopt=dec2mat(lmis,xopt,1);
K=yopt*inv(qopt);
Acl=A+Bu*K;
Ccl=C1+D1u*K;
syscl1=ss(Acl,Bw,Ccl,0);
Wc=gram(syscl1,'c');
h21=sqrt(Ccl*Wc*Ccl');
Ccl2=C2+D2u*K;
syscl2=ss(Acl,Bw,Ccl2,0);
Wc2=gram(syscl2,'c');
h23=sqrt(Ccl2*Wc2*Ccl2');
l=h21/h23;
alpha=l+2;
while (alpha<l+7)
D3=alpha*1/25;
D2=1/ms;
v=100;
i=1;
Ks1=K;
while (i<10)
    if(i>1)
    Ksi=Ks2;
    else
    Ksi=Ks1;
    end
setlmis([]);
```

```
P= lmivar(1,[4 1]);
R= lmivar(2,[2 1]);
F= lmivar(1,[1 1]);
h1= newlmi;
lmiterm([h1 1 1 P],A',1,'s');
lmiterm([h1 1 1 R],C',Ksi,'s');
lmiterm([h1 1 1 0],C1'*C1);
lmiterm([h1 1 2 P],1,Bu);
lmiterm([h1 1 2 R],-C',1);
lmiterm([h1 1 2 F],-Ksi',1);
lmiterm([h1 1 2 0],C1'*D1u);
lmiterm([h1 2 2 F],1,1,'s');
lmiterm([h1 2 2 0],D1u'*D1u);
h2=newlmi;
lmiterm([-h2 1 1 P],1,1);
h3=newlmi;
lmiterm([h3 1 1 P],A',1,'s');
lmiterm([h3 1 1 R],C',Ksi,'s');
lmiterm([h3 1 2 P],1,Bu);
lmiterm([h3 1 2 F],-Ksi',1);
lmiterm([h3 1 2 R],-C',1);
lmiterm([h3 2 2 F],1,1,'s');
lmiterm([h3 2 2 0],D3'*D3);
lmis=getlmis;
n=decnbr(lmis);
c=zeros(n,1);
 for j=1:n
    [Pj,Rj,Fj]=defcx(lmis,j,P,R,F);
    c(j)=trace(B1'*Pj*B1)+trace(B2'*Pj*B2);
end
c;
[copt1,xopt]=mincx(lmis,c);
copt1;
Ropt=dec2mat(lmis,xopt,2);
Fopt=dec2mat(lmis,xopt,3);
Kopt=inv(Fopt)*Ropt';
xopt;
setlmis([]);
P=lmivar(1,[4,1]);
Ks=lmivar(2,[1 4]);
h4=newlmi;
lmiterm([h4 1 1 P],A',1,'s');
lmiterm([h4 1 1 Ks],C'*Ropt,1,'s');
lmiterm([h4 1 1 0],C1'*C1);
lmiterm([h4 1 2 P], 1,Bu);
lmiterm([h4 1 2 -Ks], 1, -Fopt);
lmiterm([h4 1 2 0], C1'*D1u-C'*Ropt);
lmiterm([h4 2 2 0 ], D1u'*D1u+Fopt+Fopt');
h5=newlmi;
lmiterm([h5 1 1 P],A',1,'s');
lmiterm([h5 1 1 Ks],C'*Ropt,1,'s');
lmiterm([h5 1 2 P], 1,Bu);
lmiterm([h5 1 2 -Ks], 1, -Fopt);
lmiterm([h5 1 2 0], -C'*Ropt);
```

```
lmiterm([h5 2 2 0 ], D3'*D3+Fopt+Fopt');
h6=newlmi;
lmiterm([-h6 1 1 P],1,1);
newlmis=getlmis;
n=decnbr(newlmis)
c=zeros(n,1);
for j=1:n
    [Pj,Ksj]=defcx(newlmis,j,P,Ks);
    c(j)=trace(B1'*Pj*B1)+trace(B2'*Pj*B2);
end
[copt2,xopt]=mincx( newlmis,c);
copt2;
Ks2=dec2mat(newlmis,xopt,2);
v=copt1-copt2;
i=i+1;
end
Ccl3=D3/alpha*Kopt*C;
Acl=A+Bu*Kopt*C;
Ccl=C1+D1u*Kopt*C;
sys=ss(Acl,Bw,Ccl,0);
sys3=ss(Acl,Bw,Ccl3,0);
Wc=gram(sys,'c');
Wc3=gram(sys3,'c');
h221=sqrt(Ccl*Wc*Ccl');
h223=sqrt(Ccl3*Wc3*Ccl3');
if(h223>(195)&& h223<(198))
    alpha=l+7;
else
    alpha=alpha+0.02;
end
end
x(p)=Kopt(1);
y(p)=Kopt(2);
m(p)=ms;
p=p+1;
ms=ms+0.2;
end
figure(1)
plot(m,x,'x');
figure(2)
plot(m,y,'x');
```

VITA

Rohit Hari Chintala received his Bachelor of Engineering degree in mechanical engineering from Birla Institute of Technology in 2004 and 2005. Since 2008, he has been working on his graduate studies in the Department of Mechanical Engineering Department at Texas A&M University in College Station, and graduated with his M.S. in August 2011. His research interests include modeling and designing control systems.

Mr. Chintala may be reached at:

Texas A&M University
Department of Mechanical Engineering
3123 TAMU
College Station, TX 77843-3123
c/o Won-jong Kim
rohit.chintala@gmail.com